NAVAL POSTGRADUATE SCHOOL
Monterey, California

THESIS

NUCLEATION AND GROWTH OF
ANODIC ELECTROCRYSTALLIZED PRODUCTS
ON SHIP HULL ZINC IN SALT WATER SOLUTIONS
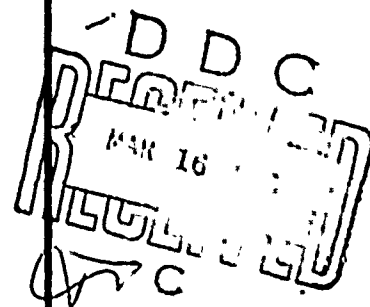
by

James M. Todd

December 1975

Thesis Advisor: A. J. Perkins

Approved for public release; distribution unlimited.

DDC

MAR 16

C

REPORT DOCUMENTATION PAGE

READ INSTRUCTIONS
BEFORE COMPLETING FORM

1. REPORT NUMBER	2. GOVT ACCESSION NO.	3. RECIPIENT'S CATALOG NUMBER

4. TITLE (and Subtitle)	5. TYPE OF REPORT & PERIOD COVERED
Nucleation and Growth of Anodic Electrocrystallized Products on Ship Hull Zinc in Salt Water Solutions.	MSME Thesis December 1975
	6. PERFORMING ORG. REPORT NUMBER

7. AUTHOR(s)	8. CONTRACT OR GRANT NUMBER(s)
James M. Todd	

9. PERFORMING ORGANIZATION NAME AND ADDRESS	10. PROGRAM ELEMENT, PROJECT, TASK AREA & WORK UNIT NUMBERS
Naval Postgraduate School Monterey, California 93940	

11. CONTROLLING OFFICE NAME AND ADDRESS	12. REPORT DATE
Naval Postgraduate School Monterey, California 93940	December 1975
	13. NUMBER OF PAGES
	175

14. MONITORING AGENCY NAME & ADDRESS(if different from Controlling Office)	15. SECURITY CLASS. (of this report)
Naval Postgraduate School Monterey, California 93940	Unclassified
	15a. DECLASSIFICATION DOWNGRADING SCHEDULE

16. DISTRIBUTION STATEMENT (of this Report)

Approved for public release; distribution unlimited.

17. DISTRIBUTION STATEMENT (of the abstract entered in Block 20, if different from Report)

18. SUPPLEMENTARY NOTES

19. KEY WORDS (Continue on reverse side if necessary and identify by block number)

20. ABSTRACT (Continue on reverse side if necessary and identify by block number)

The structure of corrosion products formed on a zinc alloy with and without a steel couple and exposed in various salt water electrolytes was studied as a function of time. A film growth mechanism is hypothesized involving nucleation of ZnO platelets in a near-surface electrolyte layer adjacent to anodic areas. Inclusion areas on the zinc surface are lead-rich corrosion product initiation points, and a passivating →

DD FORM 1473   EDITION OF 1 NOV 65 IS OBSOLETE
1 JAN 73
(Page 1)   S/N 0102-014-6601 |

1

20. Abstract (Continued)

film tends to form over these areas. Hexagonal ZnO platelets are the primary corrosion product with secondary products categorized and presented. X-ray diffraction powder patterns suggest a $ZnCO_3$ product and a $ZnCl_2$ complex product in the base film.

Nucleation and Growth of
Anodic Electrocrystallized Products
on Ship Hull Zinc in Salt Water Solutions

by

James M. Todd
Lieutenant, United States Navy
B.S., United States Merchant Marine Academy, 1968

Submitted in partial fulfillment of the
requirements for the degrees of

MASTER OF SCIENCE IN MECHANICAL ENGINEERING
and
MECHANICAL ENGINEER

from the

NAVAL POSTGRADUATE SCHOOL
December 1975

Author _____

Approved by: _____
                                        Thesis Advisor

_____
                                        Second Reader

_____
                        Chairman, Department of
                        Mechanical Engineering

_____
                                        Academic Dean

3

ABSTRACT

The structure of corrosion products formed on a zinc
alloy with and without a steel couple and exposed in
various salt water electrolytes was studied as a function
of time. A film growth mechanism is hypothesized involving
nucleation of ZnO platelets in a near-surface electrolyte
layer adjacent to anodic areas. Inclusion areas on the
zinc surface are lead-rich corrosion product initiation
points, and a passivating film tends to form over these
areas. Hexagonal ZnO platelets are the primary corrosion
product with secondary products categorized and presented.
X-ray diffraction powder patterns suggest a $ZnCO_3$ product
and a $ZnCl_2$ complex product in the base film.

TABLE OF CONTENTS

LIST OF TABLES

LIST OF ILLUSTRATIONS

9

13

LIST OF SYMBOLS

Zn	zinc
Zn^{++}	zinc ion
e	electron
E_{Zn}	zinc potential
E^o_{Zn}	standard zinc potential
R	gas constant (8.314 joules/degree $\cdot$ mole)
T	temperature
n	number of electrons in cell reaction (faraday/mole)
F	faraday constant (96,500 coulombs)
$a_{Zn^{++}}$	zinc ion activity
H^+	hydrogen ion
O_2	oxygen
H_2O	water
E_D	cathode potential
E_D^o	standard cathode potential
a_{H^+}	hydrogen ion activity
P_{O_2}	oxygen activity
OH^-	hydroxide ion
E_{O_2}	oxygen potential
$E^o_{O_2}$	standard oxygen potential
a_{OH^-}	hydroxide ion activity

emf	electromotive force
FeSi	iron silicide
ppm	parts per million
Fe_2Al_5	iron aluminide
cm^2	square centimeter
μm	micrometer
ZnO	zinc oxide
ml	milliliter
l	liter
pH	standard hydrogen potential ($pH = -\log A_H^+$)
A	Arrhenius constant
B	activation energy
exp	base of natural logarithms
C	centigrade degrees
t	time
cm	centimeter
SEM	scanning electron microscope
$ZnCO_3$	zinc carbonate
$ZnCl_2$	zinc chloride
$Zn(OH)_2$	zinc hydroxide
Cl	chlorine
Pb	lead
Fe	iron

Al	aluminum
Cr	chromium
Si	silicon
d	atomic spacing
$\overset{o}{A}$	Angstrom units

ACKNOWLEDGEMENT

The author wishes to express his appreciation to Professor A. J. Perkins for his guidance and encouragement during the course of this investigation. The impetus for this investigation was provided by the sponsorship of the Department of Mechanical Engineering, NPGS, Monterey, California.

A special note of thanks is due to Roy Edwards, Material Science Laboratory Technician, whose untiring assistance throughout the course of the investigation was invaluable to the author.

I. INTRODUCTION

A. CATHODIC PROTECTION

Corrosion of metals in an environment such as sea water
is of an electrochemical nature. Electrochemical corrosion
consists of chemical reaction accompanied by passage of
electrical current. [1] In order for this to occur a
potential difference must exist between different metallic
areas in the system. Anodes exist at areas of lower
reduction potential where dissolution of metal occurs by
the loss of electrons (oxidation) to form ions. Cathodes
exist at areas of higher reduction potential where the
anode   ctrons migrate to be utilized in a
reductio   The reduction process can take a variety
of forms. The combination of the anodic and cathodic pro-
cesses causes the passage of current via electrons in the
solid metallic areas and electrolytic conduction via ions
in solution. In most cases of single metal corrosion, the
galvanic cell is made up of microscopic anode and cathode
areas distributed over the surface of the metal.

The electrochemical microcell corrosion model is well
established in the literature [2] and shows zinc going into
solution at an anode site:

19

$$Zn \longrightarrow Zn^{++} + 2e^-$$

with the reversible half-cell potential given by

$$E_{Zn} = E^O_{Zn} - \frac{RT}{nF} \ln a_{Zn^{++}}$$

The above anode reaction leaves the surface of zinc spotted with "pits" at anode sites by a chemical dissolution process. To balance the electronic charge requirements, electrons are accepted at cathode sites by one of the following reactions:

$$2e^- + 2H^+ + \tfrac{1}{2} O_2 \longrightarrow H_2O \tag{1a}$$
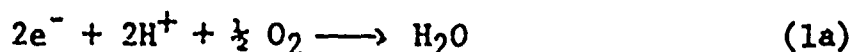
where

$$E_D = E^O_D - \frac{RT}{2F} \ln \frac{1}{(a_H^+)^2 \, (p_{O_2})^{\frac{1}{2}}} \tag{1b}$$

in acidic solutions, or

$$2e^- + \tfrac{1}{2}O_2 + H_2O \longrightarrow 2(OH)^- \tag{2a}$$
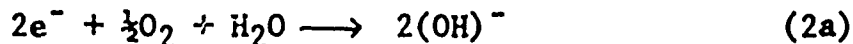
where

$$E_{O_2} = E^O_{O_2} - \frac{RT}{2F} \ln \frac{(a_{OH}^-)^2}{(p_{O_2})^{\frac{1}{2}}} \tag{2b}$$

in neutral or alkaline solutions.

Equations 1a and 2a are exactly equal in overall electrode emf; consequently, it is futile to distinguish between these two expressions chemically. These equations show favored reactions in the presence of oxygen.

Cathodic protection utilizes a principal which is the application of a counter-current sufficiently large to neutralize the dissolution process at the microanode areas,

so that the metal as a whole acts as a cathode and is protected. The type of cathodic protection to be discussed in this thesis is galvanic coupling utilizing an electrode of sacrificial metal which is anodic with respect to the metal to be protected.

Before discussing galvanic coupling, some description of the other type of cathodic protection, namely impressed current, is appropriate. [3] In this case, the counter-current source to the corroding metal is an electrode that becomes the anode. The anode material used here can be either an inert material or one that deteriorates and is replaced periodically. One reason this type of cathodic protection is not being utilized as the major cathodic protection system for the protection of U.S. Navy ship hulls is that a dedicated direct current power source or a set of silicon type rectifiers with associated circuit equipment as well as control system equipment is both expensive and space consuming compared to the galvanic sacrificial anode system. Typical impressed current anode materials are scrap iron, silicon-iron, carbon, stainless steel, and platinum. Impressed current cathodic protection systems do offer potentially better cathodic protection over the long haul than galvanic anodes, but the factors stated above plus

the added maintenance required by ship's force personnel
have kept this system from being fully exploited.

Galvanic coupling utilizes metals with uniquely different
electrode potentials in order to automatically insure an
appropriate anti-corrosion current for the cathode metal.
Metals have been classified according to relative electrode
potentials in a standard galvanic series. The more electro-
negative metals (on a standard reduction potential scale)
are commonly used as sacrificial anodes because they are
able to supply a sufficient counter-current to neutralize
the corrosion current. Magnesium, zinc and aluminum are
the metals most commonly used as sacrificial anodes for
cathodic protection.

Magnesium has been utilized on ship hulls as a galvanic
anode. In fact, magnesium is more electronegative than any
of the metals in the galvanic series, but magnesium anodes
are only 50% efficient in sea water. This means that half
the anode deteriorates in sea water without providing any
useful protective current. In addition, the high potential
of magnesium necessitates the use of dielectric shields on
the hull beneath and at least two feet around the periphery
of the anode array. Severe paint damage and subsequent loss
of the system's effectiveness can occur without this shielding.

The paint damage is due to hydrogen evolution from the magnesium dissolution process and is a major disadvantage of using this metal on ship hulls. The replacement cycle for magnesium anodes in sea water is two years.

Aluminum's virtues as a galvanic anode are its relative light weight and its ability to provide more than three times the current per pound compared to zinc anodes. Since equivalent surface areas of zinc and aluminum have approximately the same current outputs and the efficiency of aluminum anodes in sea water is greater than 90%, it is possible to design a system utilizing aluminum which would weigh the same as zinc but would only require replacement every six years. The only problem seems to be in development of an alloy with reliable service characteristics. Experimental evidence indicates that aluminum corrosion morphology is very sensitive to small changes in many ordinary metallurgical variables such as grain size, heat treatment, and impurities.

Zinc is the most widely used anode material for cathodic protection of U.S. Navy ships and is currently installed on 90% of the ships. It is over 90% efficient in sea water and has a replacement cycle of three years. The U.S. Navy procures zinc anodes under military specification MIL-A-18001H.

Much investigative work has been done to discover an optimum zinc anode.

Galvanic coupling utilizes a process whereby the effect of coupling zinc with steel hulls is to cause the steel to become a local cathodic electrode while the zinc becomes an anodic electrode. The zinc "sacrifices" itself by dissolution, forming zinc ions which become part of the electrolyte. As long as the zinc continues to function as an effective anode, the steel will not corrode. If, however, a dense corrosion film forms on the zinc anode, the electrolyte will be unable to penetrate to the metal surface and zinc will not be able to deliver the counter-current required to make it an effective anode. This condition is referred to as passivation.

Historically, the use of zinc anodes for cathodic protection dates back to 1824 when Sir Humphrey Davy [4] advised the British Admiralty to use blocks of zinc to protect the copper sheathing on Admiralty ships. Subsequently, zinc anodes were used on other structures, such as steel-hulled ships, buoys, and steel pilings, to protect them from galvanic attack.

Around 1940, separate investigations were conducted by the British Admiralty and the U.S. Navy as a result of

problems encountered with in-service use of zinc anodes on ships' steel hulls. One of the results of these investigations stated that "the current output of zinc anodes in sea water is restricted, after a short period of time, by the formation of tightly adherent corrosion product films." [5]

The 1950's and 1960's found many investigations attempting to discover the cause of adherent film formation on zinc anodes in sea water. R. B. Teel and D. B. Anderson [6] reported in 1956 that iron content in zinc anodes when found to be greater than 0.0014% had a pronounced effect on both decreased current output and the formation of adherent product film. Even more interesting'y, they reported that: "The corrosion products present on the zinc were made up of two distinct layers. The outer layer contained mounds of corrosion products which were located directly over pitted areas on the surface of the zincs. The inner layer was more dense and contained an adherent black deposit that appeared in greater quantities on the zincs containing the greater amount of iron."

Other investigators later discovered that al: ing certain other elements with zinc tended to counteract the adverse effects of iron. Southin [7] reported that iron, which has a low solid solubility in zinc, appears in the

25

microstructure as an iron-zinc compound containing 6% iron when it is present in amounts greater than 10ppm. A relatively large amount of the 6% iron-zinc compound is found in zinc anodes containing as small as 0.07% iron. He reported that adding silicon causes the formation of FeSi which is resistant to corrosion and therefore unlikely to take part in the corrosion process. The formation of this compound reduces the amount of 6% "free" iron to a very low level of less than 5ppm. One problem associated with adding silicon to zinc castings is that silicon has a very low solubility in liquid zinc necessitating an aluminum-silicon alloy which is soluble in liquid zinc. Aluminum [7] is also beneficial to zinc anode performance because it goes into solid solution and has been found to make the corrosion product less adherent or more porous. It also affects grain size but Southin [7] reported that grain size does not affect anode performance. Aluminum has another beneficial effect in that it causes the formation of Fe_2Al_5 which reduces the 6% "free" iron in much the same manner as silicon. Cadmium [7] is another element added to zinc anodes which has good solid solubility characteristics and also tends to change the corrosion product composition, making it less adherent.

The conclusion [7] reached from the above discussion of elemental additions to zinc anodes is that there are two

available complementary mechanisms which can lead to improved performance of alloyed zinc anodes:

1. The addition of elements which reduce the 6% "free" iron present in iron-zinc alloys by the formation of a compound which takes no part in the corrosion process. Examples of this are FeSi and Fe_2Al_5.

2. The addition of elements which have some solid solubility in zinc. This improves anode performance by changing the composition of the corrosion product by making it less adherent. More future improvements are possible in this area.

One might conclude from the above discussion that the best way to ensure good zinc anode performance is to go to extremely high purity zinc, eliminating other elements entirely. However, Waldron and Peterson [8] investigated this very possibility and reported that anode performance was markedly superior for those anodes which had certain optimum amounts of aluminum and cadmium as compared to extremely high purity zinc anodes, with iron content maximum at .0014% and constant in both samples. These results, as well as work by Carson [9] and his colleagues, have led to recommended optimum percentages for each of the elements discussed above. The U.S. Navy has generally adopted the results of these investigations in determining specifications

27

for elemental content of alloy zinc anodes used on ship hulls for cathodic protection.

Since the early 1960's, very little can be found in the literature which sheds further insight into the reason why iron impurities in zinc anodes may cause the formation of strongly adherent corrosion-products during sea water galvanic corrosion. U.S. Navy service experience in recent years occasionally has found dense adherent film formations on hull zincs without proper explanation of the cause. Directives in the early 1970's concerning the use of zinc anodes in heat exchanges and condensers on U.S. Navy ships ran the gamut from complete removal to partial reinstallation.

Knowledge has never been developed regarding microscale mechanisms leading to the effectiveness of zinc anodes. In view of this need for a better understanding of the nature of anodic zinc corrosion, Perkins and Bornholdt [10, 11] initiated studies at the Naval Postgraduate School in 1973 which also formed the basis for the present study. Utilizing standard Naval specification zinc specimens and direct microscopic examination of corrosion product morphology, Bornholdt and Perkins observed that the anodic film structure for zinc-steel couples in sea water was a microscopically porous

formation of discrete single crystal hexagonal shaped
platelets of zinc oxide. [11] The density of the zinc
oxide platelets was on the order of 10^6 platelets per cm^2
of anode surface, and individual platelets grew to about
30 μm diameter and several μm thickness after one week
exposure. One other important detail observed was that
the zinc oxide platelets tend to form with the ZnO basal
plane of the hexagonal ZnO crystals parallel to the broad
slow-growing faces, with these faces tending to be at high
angles (nearly right angles) to the anode surface. Extension
of these studies by this student has sought to delineate the
details of the film nucleation and growth process on zinc
anodes and to relate particular variations to base metal
structure and environmental conditions, with the ultimate
aim of testing the significance and necessity of current
compositional specifications for zinc anode materials.

B. CORROSION VARIABLES

Passivation has many definitions in corrosion literature,
but in this study passivation will be defined as the phen-
omenon which occurs when the corrosion film formation is so
thick and adherent that the anode ceases to act as an
effective anodic cell in a cathodic protection system.
Before actually describing the experimental procedures used

to pursue the zinc corrosion product morphology and passivating film formation mechanisms on zinc anodes, some discussion of the variables affecting zinc corrosion in sea water seems appropriate.

1. Composition of the environment: Probably the most difficult aspect of the corrosion process to duplicate consistently in the laboratory is the ocean environment. Sea water is a complex heterogeneous mixture. It is composed of water, a multitude of dissolved gases and salts, suspended organic and inorganic matter, and live organisms. When these variables are considered along with wide variations in temperature, pressure, and current velocity, it becomes obvious that one must evaluate corrosion in specific ocean regimes rather than expect to be able to extrapolate results obtained from laboratory solution tests. Monney [12] reported that salinity variations in the open ocean are relatively small and generally range in value between 33 to 35 parts per thousand. Therefore, salinity variations should not influence corrosion rates by more than 10% to 15%. Live organisms [12] which can influence corrosion rates by the formation of oxygen concentration cells exist at all ocean levels. They are much more numerous and troublesome in warm, oxygen rich surface waters. Sea water

30

is observed [12] to be slightly basic, with a nearly

constant pH ranging in value from 8.0 to 8.3 near the

surface. This knowledge of the pH range is very important

in corrosion studies and is a major variable effecting

passivation potential. The oxygen content of sea water is

a vital determinant in corrosion rates. Near the surface,

the oxygen content is generally in the range of from 4 to

7 ml of dissolved gas at standard temperature and pressure

per l of water and decreases with depth. In general,

corrosion rates decrease as oxygen content decreases, but

pitting and crevice corrosion can still occur.

2. Temperature: In most cases, increasing temperature

increases the severity of corrosion. This can be illustrated

by the well-known Arrhenius equation:

Rate of Corrosion = A exp (-B/RT)

where all the symbols except T are constants; T is absolute

temperature, B is activation energy, R is the gas constant

and exp is the base of natural logarithms. This relation-

ship may break down at temperatures above $60^\circ C$ where there

is evidence [13] that the anode-cathode potentials for zinc-

iron couples reverse making the iron anodic to zinc.

Depending on the activation energy, the rate of a chemical

reaction can double with an increase in temperature of only

10°C. [12] Also the conductivity of sea water nearly doubles as the temperature is raised from 0° to 25°C. Zinc anodes ordinarily will experience a temperature range in service of approximately 0° to 30°C.

3. Velocity: Most corrosion products which form on a surface inhibit corrosion. If they are soft, currents may wash them away and increase the corrosion rate. Also, if the cathodic process is controlled by ion concentration polarization, removal of the ion concentration by currents will increase the corrosion rate. The former velocity effect is extremely important in evaluating in-service anode performance. It can be assumed from this characteristic alone that ship hull zinc anodes will not tend to passivate while the ship is underway. Therefore, passivation of current military specification anodes is actually only a severe problem for ships which are in port for periods in excess of one week.

4. State of stress: Zinc anodes are not subjected to any appreciable stress states in service other than those transient gradients due to propellor wash and ship velocity. Therefore, this variable is not a very important one in evaluating zinc anode performance and corrosion product morphology.

5. Time: Corrosion rates are all time dependent. Therefore, this variable is of great importance to any corrosion

study. In this study, the actual corrosion process on zinc
anodes as a function of time was closely studied.

6. Chemical composition of the metal: In light of the
discussion above concerning the effect of alloying elements
on the corrosion film formation of zinc, the chemical
composition of zinc is an extremely important variable. The
zinc anode material utilized in this study was obtained from
Mare Island Naval Shipyard and was military specification
Mil-A-18001H /14/ anode material of the type currently in
use on U.S. Navy ships. Table I shows the chemical composi-
tion of these anodes.

7. Degree of homogeneity of the alloy: Local anodic/
cathodic cells can be formed on the surface of zinc due to
differences in elemental composition. This variable is
believed to be quite significant with regard to passivation
of zinc anodes and is the issue primarily addressed in this
study.

8. Pressure: This variable has some effect on the ·
corrosion process. Primarily, pressure affects the concen-
tration of ocean environmental variables. This has been
investigated separately /15/ and will not be addressed in
the present study.

·

II. EXPERIMENTAL PROCEDURES

Corrosion tests were conducted in the laboratory using
zinc samples 1.25 cm x 1.25 cm x 0.6 cm in size. The zinc
alloy was 99.9907% pure zinc, adhering in most respects to
Mil-A-18001H [14] (see Table I). The test assembly consisted
of 2000ml beakers filled with 1800ml of electrolyte (see
Figure 1). Three different electrolytes were used in the
experiments. One of these was natural sea water from
Monterey Bay with a salinity of 32.8 to 33.8 parts per
thousand and an oxygen content of 1.33 ml/liter. In addition,
synthetic sea water conforming to ASTM-D1141-52 (see Appendix
A and Table II) standards was prepared and used. Distilled
water was the third electrolyte. In most of the tests the
zinc samples were coupled to a low carbon steel plate with
an area ratio of the couple (cathode to anode) at approxi-
mately 50-1 which closely conforms to standard U.S. Navy
service requirements for cathodic protection.

Great care was taken to prepare the zinc samples in an
effort to show reproducibility of data. The samples were
washed in acetone, rinsed in distilled water, ground on two
different SiC grit paper in order to get as finely a polished
surface as possible, and rinsed in distilled water again.

34
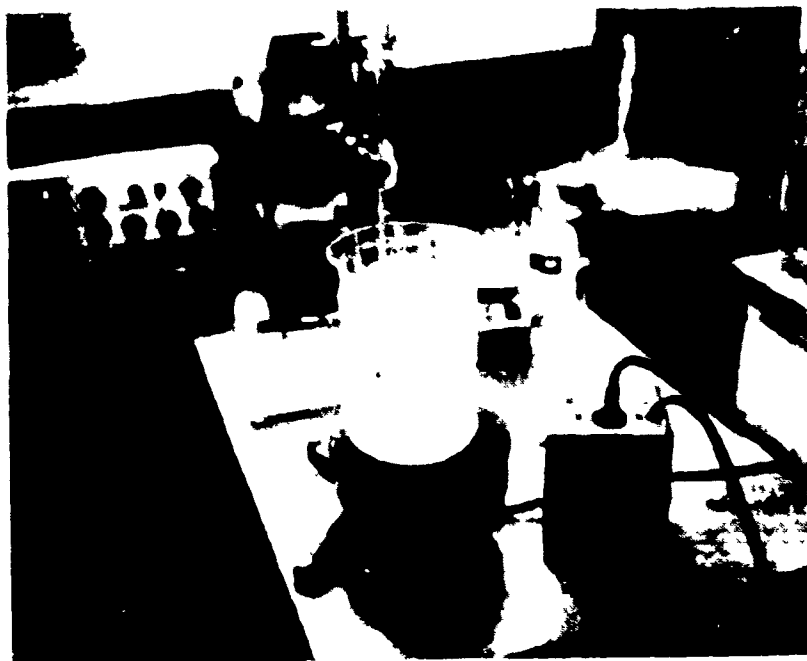
Figure 1

2000ml beaker used in corrosion tests

Each sample was prepared as nearly the same as possible. Figure 2 shows a clean polished zinc surface at 3000X magnification, which illustrates the typical initial surface condition of zinc samples used in these experiments. When the samples were coupled with zinc, the steel was always ground and free of rust. Nylon bolts attached to a specially designed plexiglass stand were used to couple the zinc and steel (see Figure 3).

The zinc was corroded in a number of different ways. Samples were immersed in distilled water or in natural sea water, with and without steel coupling, or were coupled with steel in synthetic sea water (referred to here as lab sea water).

After exposure, each zinc sample was rinsed in distilled water, dried in air, and mounted on a SEM stub. Each sample was examined for corrosion film morphology utilizing a Cambridge Model S4-10 scanning electron microscope (SEM) (see Appendix B and Figure 4).

Use of the SEM allows observation of surface corrosion film growth at a useful magnification up to about 10,000X. Most microphotographs in this study were taken at about 2500X. Generally, microphotographs were made of areas on each sample representative of the most often observed pattern
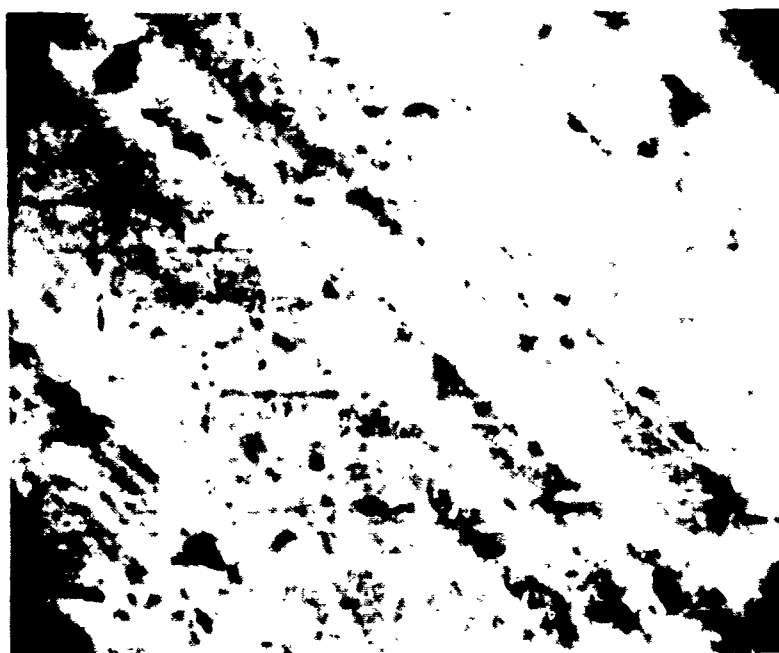
Figure 2

Scanning electron microphotograph of
initial polished zinc surface, 3000X
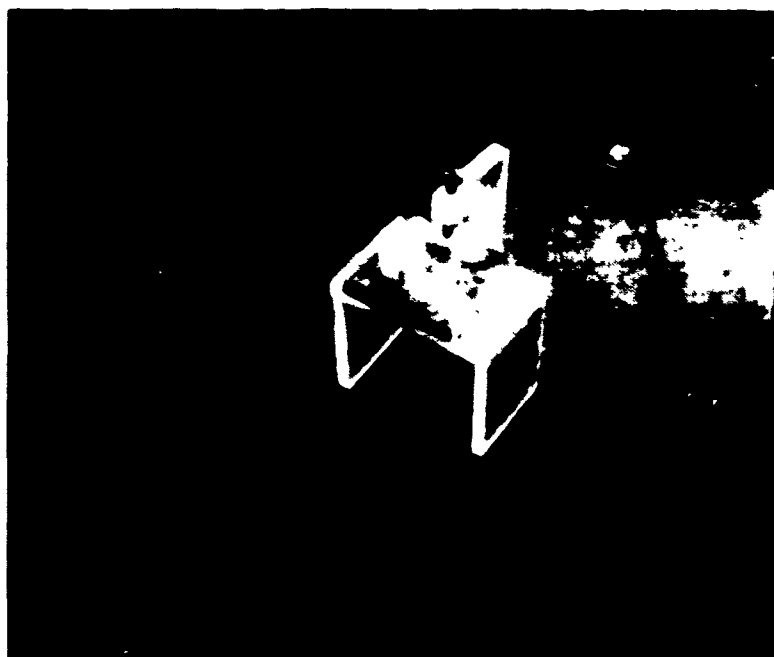
Figure 3

Plexiglass stand assembly with steel
plate and zinc anode sample
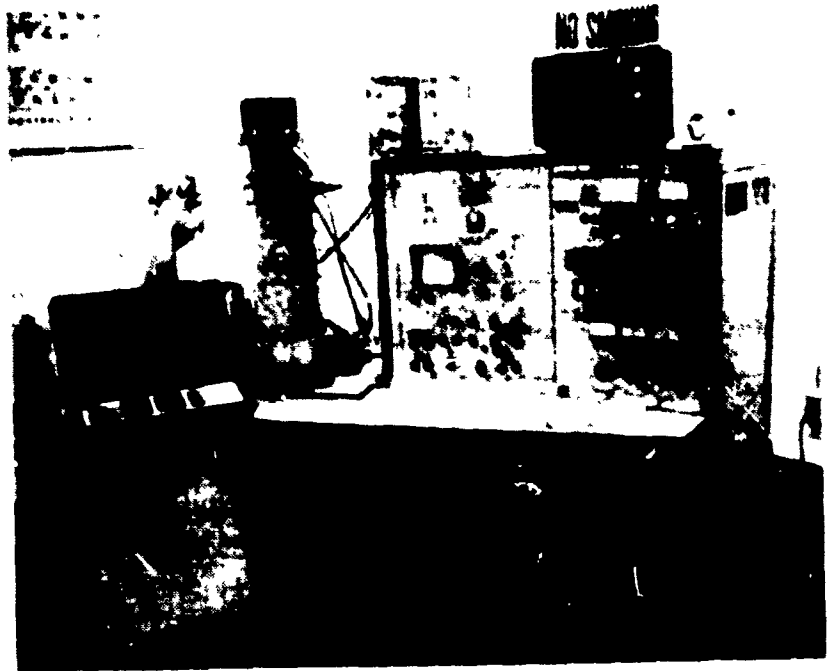
Figure 4

Cambridge Model S4-10 scanning electron
microscope (SEM) and Princeton Gamma-
Tech PGT-1000 X-ray Analyzer

of the corrosion film, as well as locally unique film forma-
tions.

While nearly all exposures were at room temperature, a
series of tests were conducted at $50^{\circ}C$ for steel-coupled
zinc samples in lab sea water.

Selected samples were pre-etched in a chromic acid solu-
tion (see Appendix C).

Selected samples for all the above conditions were
investigated for surface elemental content utilizing the
PGT-1000 non-dispersive X-ray spectrometer. This equipment
allows high resolution X-ray elemental analysis of corrosion
products of interest. The operating principles of the PGT-
1000 are discussed in Appendix B. It seems appropriate,
however, to point out some of the more useful characteristics
and features of the spectrum analysis. Each element emits
X-rays at a distinct energy level; the analyzer displays an
energy spectrum, and individual elements can be identified
at the various peak intensities; this identification feature
is a programmed function of the PGT-1000. Figure 5 shows
the spectrum generally seen when analyzing clean zinc surface
areas illustrated previously in Figure 2. The three distinc-
tive peaks in Figure 5 are identified as zinc peaks by the
analyzer element identification program, and this feature is
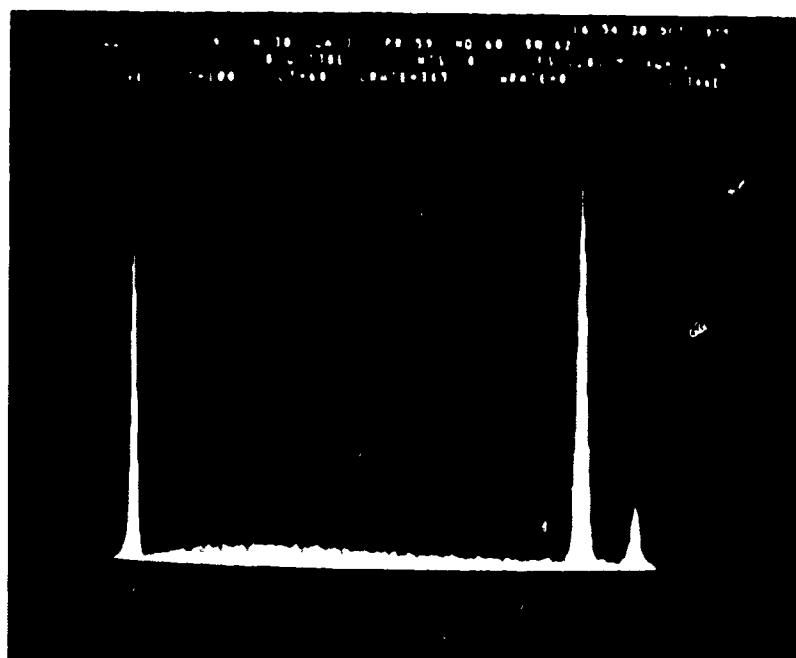
Figure 5

X-ray spectrum of clean Zn surface

shown in Figure 6. The command of "Lines 30" seen in the upper left-hand corner of the spectrum photograph results in the lines shown in Figure 6; and the element number 30, Zn, is shown in the upper right-hand corner just below the date. All future discussion or identification of elemental impurities in the corrosion product morphology will have resulted from a procedure like the one described above.
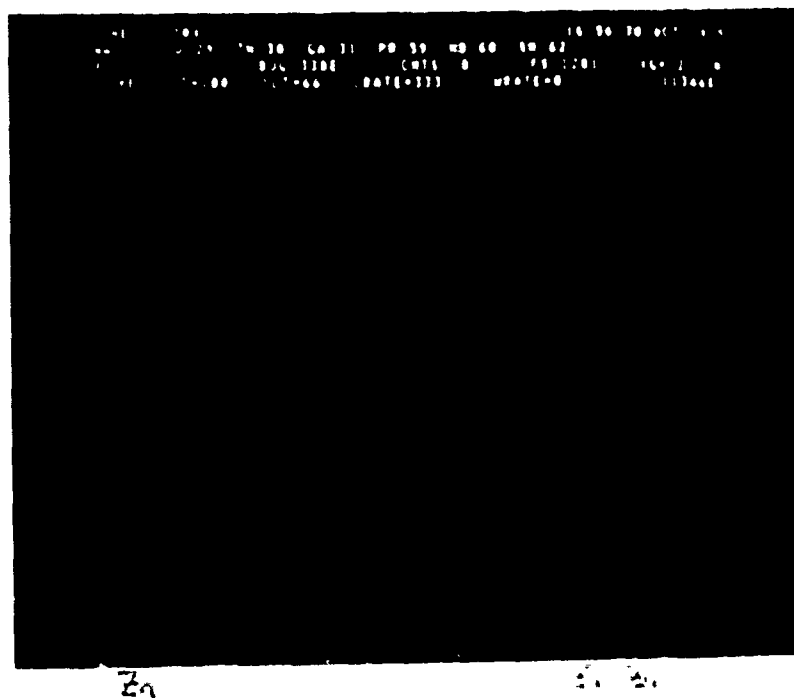
Figure 6

X-ray spectrum of clean zinc surface
showing elemental Zn lines in the spectrum

43

III. EXPERIMENTAL RESULTS

A. DISTILLED WATER TESTS

SEM examination of samples immersed in distilled water
without steel couples for various time periods up to 24
hours showed very little corrosion product formation. A
few starburst-like oxide deposits were found as well as
round, black areas. Samples coupled with steel and immersed
in distilled water for various time intervals up to 36 hours
also exhibited these round, black zones and starburst cluster-
type zinc oxide formation. The round areas are larger and
the clusters more numerous in the coupled samples for the
same time exposure. Figures 7 and 8 show th.; general surface
conditions at 129X magnification and the oxide cluster forma-
tion at 2600X magnification, respectively, of a sample
exposed for $2\frac{1}{2}$ hours. Of particular interest in Figure 7
are the dark round areas. These are relatively more-
conducting zones and seem to have at their center some sort
of surface impurity. Investigation of one of these areas
utilizing the PGT-1000 X-ray analyzer yields an energy
spectrum shown in Figure 9 which has distinct peaks for
zinc, lead and chlorine.

Figure 7

Zinc anode surface corroded in distilled
water electrolyte, steel couple, 2.5
hours exposure, 130X

Figure 8

Oxide cluster formation on steel
coupled zinc anode in distilled water
electrolyte, 2.5 hours exposure, 2600X
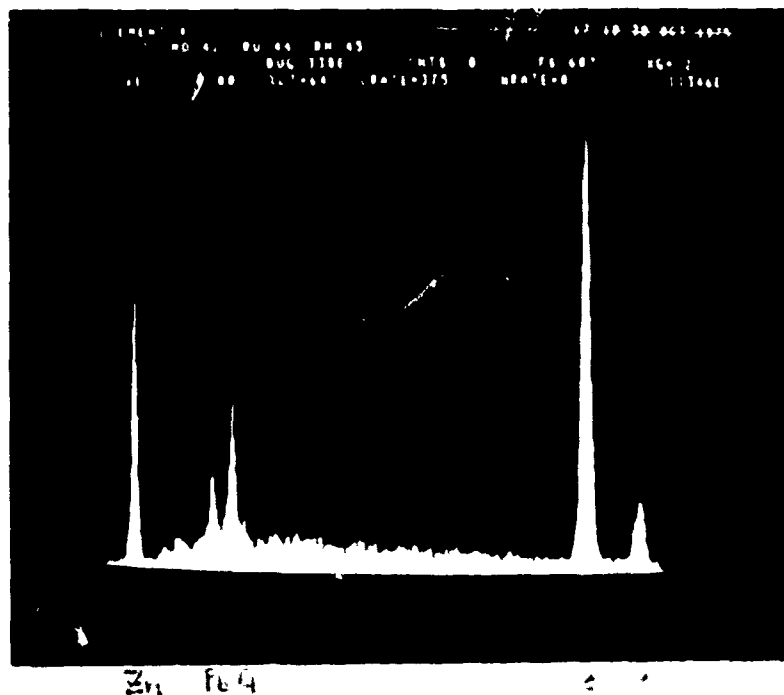
Figure 9

X-ray spectrum of "dark" area showing
zinc, lead, and chlorine peaks for
zinc anode, distilled water electrolyte,
steel couple, 2.5 hours exposure

B. SEA WATER TESTS

Figure 10 shows the result for uncoupled exposure in
sea water electrolyte for an exposure time of 24 hours.
The corrosion product is not very dense with cluster forma-
tion of zinc oxide platelets as well as a few single plate-
lets. General surface corrosion is not evident.

The nucleation and growth kinetics of the oxide formation
in the exposures described above were not the same as for
zinc samples coupled with steel in sea water. However, the
observance of surface impurities and their effect on the
corrosion morphology in the early stages suggested that close
attention should be paid to this aspect of the phenomenon of
oxide crystal growth on zinc protective anodes. The oxide
film morphology on coupled samples at exposure times up to
one hour was extensively studied on the SEM. Figures 11,
12, 13, 14, 15 and 16 show the corrosion product morphology
formation (all at 2500X magnification) after 10, 12, 15, 20,
25 and 30 minutes exposure respectively. Of particular
interest on these microphotographs is the progressive nuclea-
tion and growth mechanism. Duplicate tests to those above
using lab sea water produced nearly identical nucleation and
growth results. Figure 17 illustrates growth versus time
results up to one hour for the tests described above.

Figure 10

Base ZnO platelet formation on
uncoupled zinc anode in natural sea water
electrolyte, 24 hours exposure, 2600X

Figure 11

Anode surface appearance on steel
coupled sample in natural sea water
electrolyte, 10 minutes exposure, 2500X

Figure 12

Anode surface appearance on steel
coupled sample in natural sea water
electrolyte, 12 minutes exposure, 2500X

51
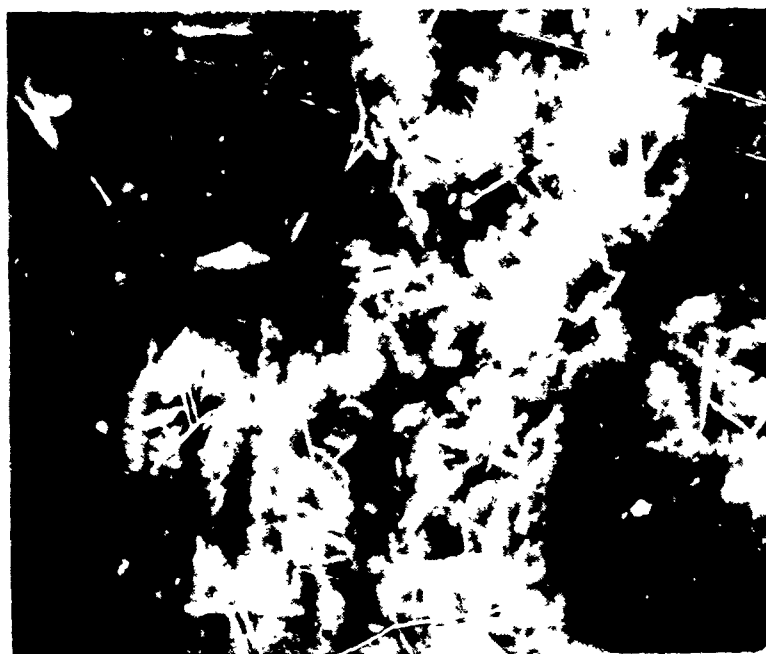
Figure 13

Anode surface appearance on steel
coupled sample in natural sea water
electrolyte, 15 minutes exposure, 2500X
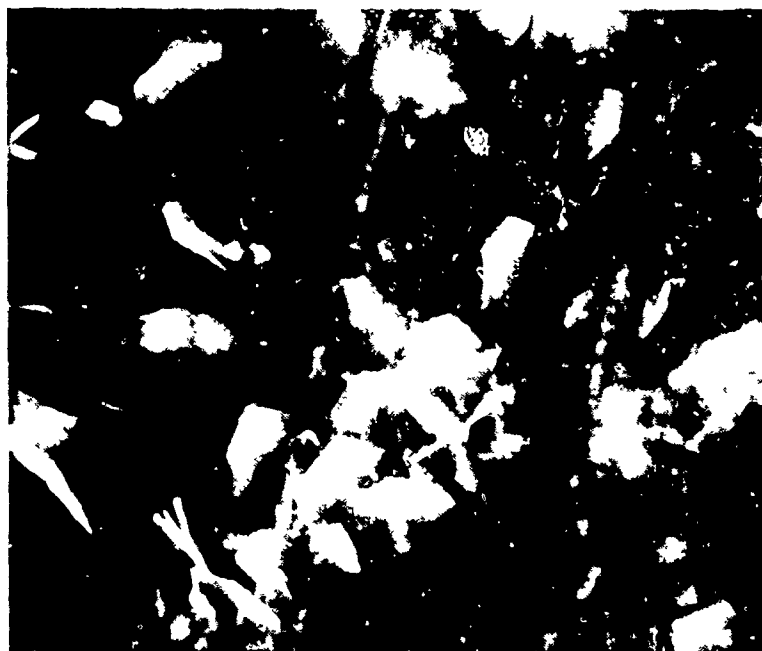
Figure 14

Anode surface appearance on steel
coupled sample in natural sea water
electrolyte, 20 minutes exposure, 2500X

Figure 15

Anode surface appearance on steel
coupled sample in natural sea water
electrolyte, 25 minutes exposure, 2500X
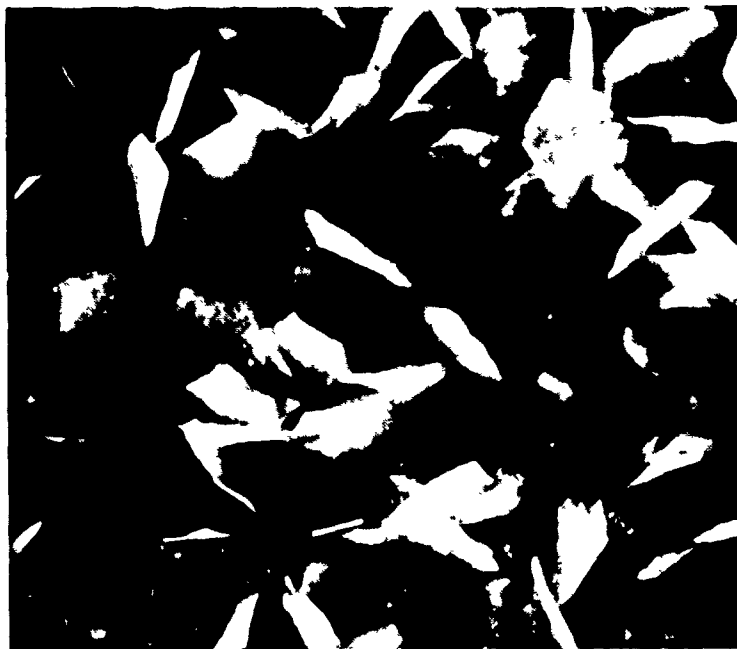
Figure 16

Anode surface appearance on steel
coupled sample in natural sea watrr
electrolyte, 30 minutes exposure, 2500X
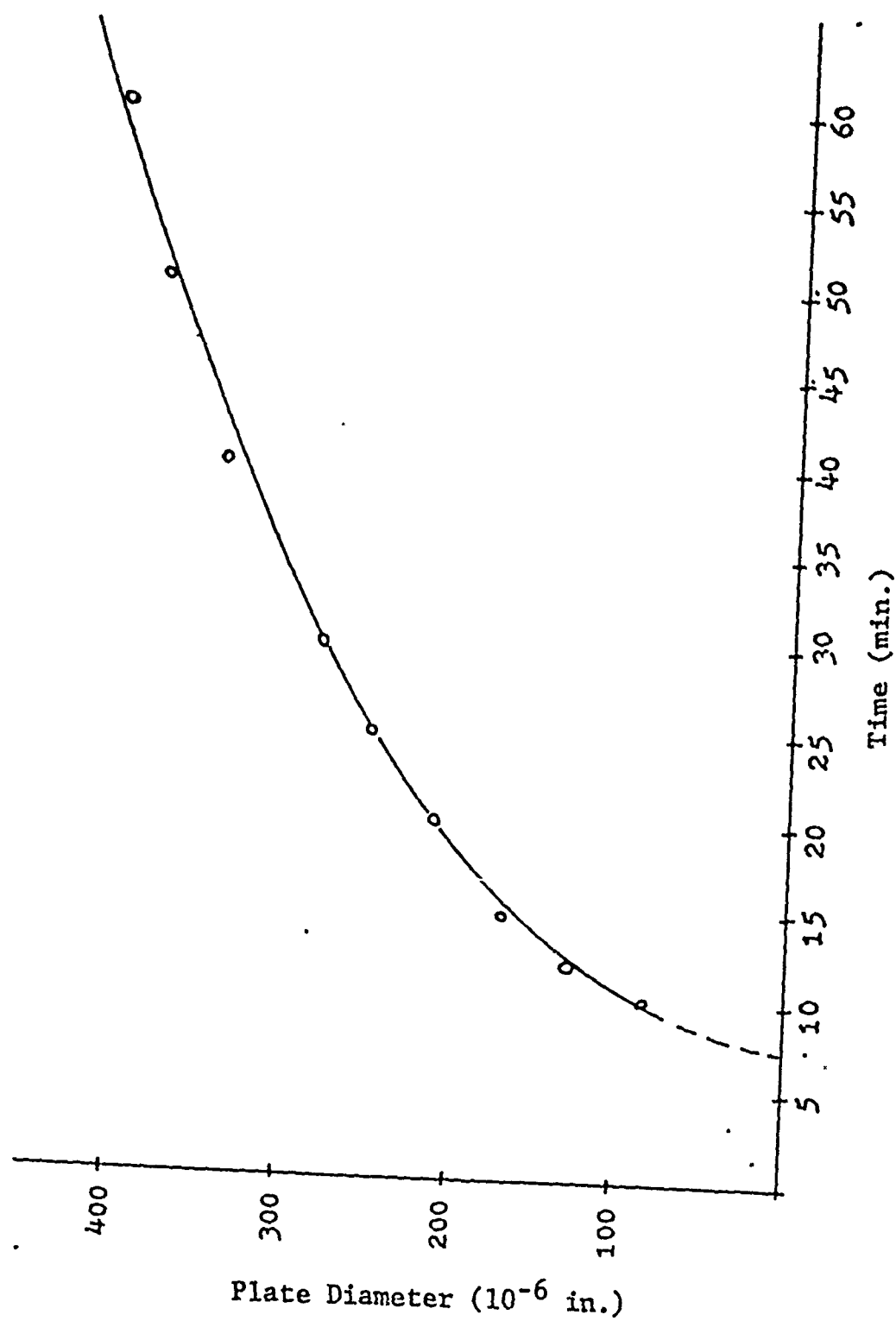
Figure 17

Maximum ZnO platelet diameter versus time exposure

A parallel series of tests were conducted at conditions
identical to those described above for steel coupled, sea
water electrolyte samples but at 50°C versus room temperature
of 25°C. The results of these tests are shown in Figures
18, 19, 20, 21 and 22 which show progressive nucleation and
growth for time exposures of 3, 5, 10, 15 and 22 minutes
respectively. The effect of higher temperature conditions
is simply to shift the growth rate curve in Figure 17 to
the left since although nucleation occurs earlier, it
progresses as before under room temperature conditions. No
significant change in the corrosion product morphology was
observed at the higher temperature exposures.

Some samples exposed under these static conditions at
room temperature produced a passivating film after about a
week as shown in Figure 23. It was observed that those
samples with passivating film formations had dense oxide
film growth over surface areas which exhibited some sort
of elemental impurity. Figure 24 is a good example of the
oxide cluster formation growth preference over the "dark"
areas in the microphotograph.

C. PRE-ETCHED SAMPLES

The evidence of corrosion product initiation and accumula-
tion at "dark" areas on the zinc anode surface suggested a

Figure 18

Anode surface appearance on steel
coupled sample in natural sea water
at 50°C, 3 minutes exposure, 2500X
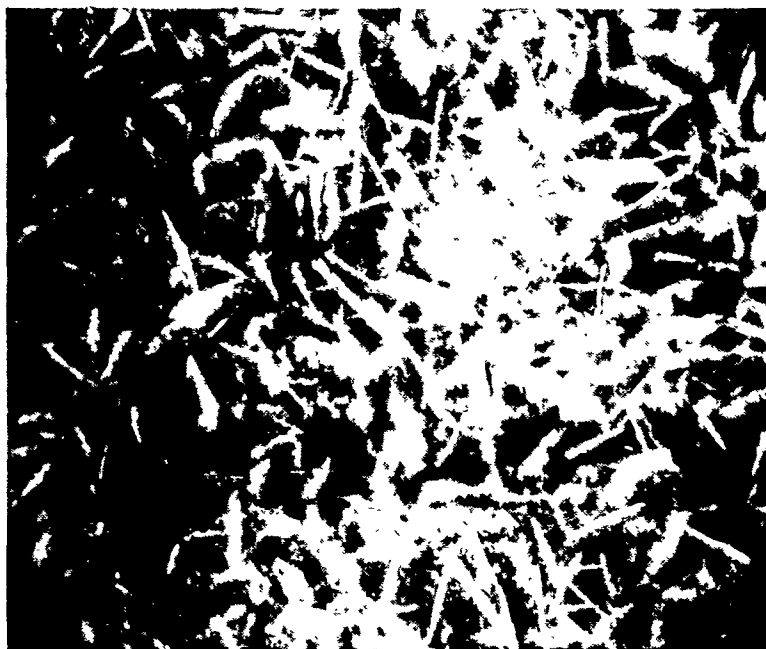
Figure 19

Anode surface appearance on steel
coupled sample in natural sea water
at 50°C, 5 minutes exposure, 2500X
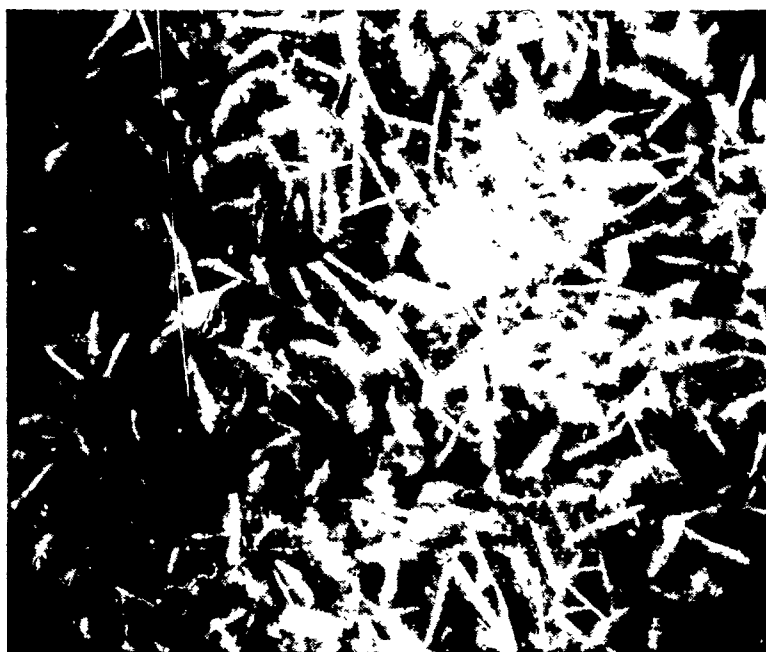
Figure 19

Anode surface appearance on steel
coupled sample in natural sea water
at $50^{\circ}C$, 5 minutes exposure, 2500X

Figure 20

Anode surface appearance on steel
coupled sample in natural sea water
at $50^{\circ}C$, 10 minutes exposure, 2500X
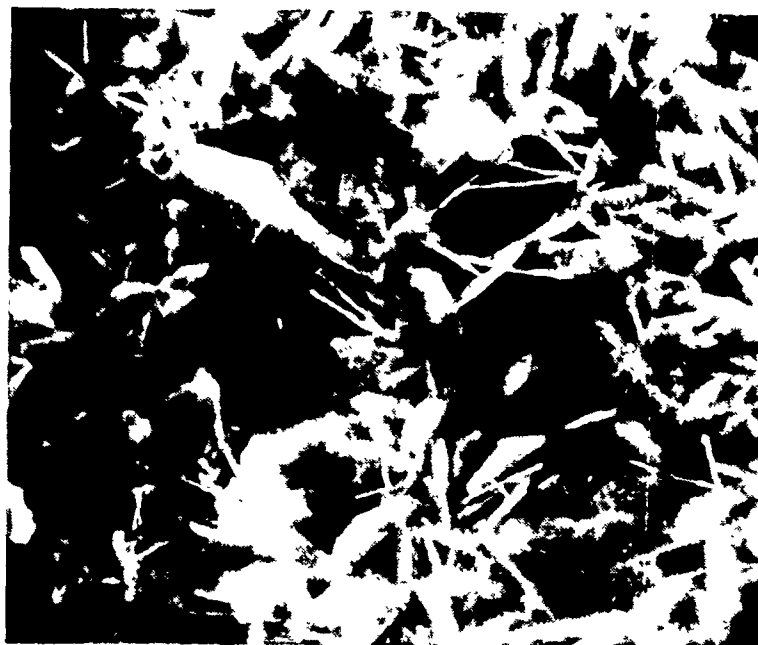
Figure 21

Anode surface appearance on steel
coupled sample in natural sea water
at 50^OC, 15 minutes exposure, 1280X

Figure 22

Anode surface appearance on steel
coupled sample in natural sea water
at 50°C, 22 minutes exposure, 1280X

Figure 23

Passivating film growth on steel
coupled sample in natural sea water
electrolyte, 1 week exposure, 250X
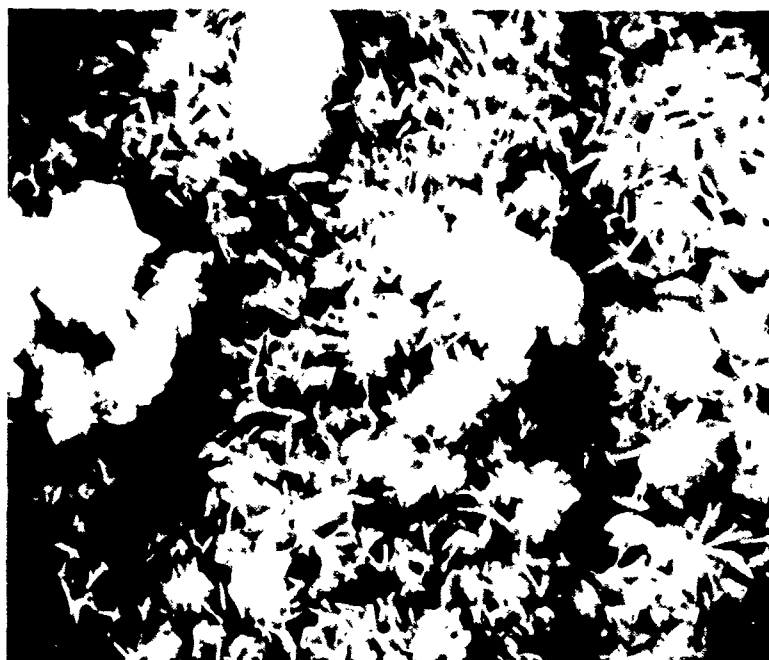
Figure 24

Oxide cluster formation over "dark"
areas on steel coupled sample in
synthetic sea water electrolyte,
4 hours exposure, 680X

more detailed look at the surface features. Pre-etching was used (see Appendix C) since the grain structure and orientation were of interest. Figures 25 and 26 illustrate a clean zinc etch at 1260X and 2700X respectively. The "dark" areas are generally distributed over the zinc surface and can be explained as elemental inclusions in the zinc cast. An X-ray spectrum analysis of the inclusion spots is shown in Figure 27. Zinc peaks are dominant as well as a peak which is identified by the analyzer as lead. Figure 28 is another microphotograph of the grain structure and an inclusion area which had oxidized. Other samples were etched and subsequently coupled to steel and immersed in sea water electrolyte. Figures 29, 30, 31 and 32 show the results of a 30 minute immersion in lab sea water. It is interesting to note in Figures 31 and 32 the apparent randomness of the zinc oxide platelets as they are attached to the base zinc and the "pitted" appearance of the base zinc. Figure 29 shows the inclusion areas have dissolved to larger holes when compared to clean zinc inclusion areas in Figure 25. Figure 30 is a higher magnification view of an inclusion area (3000X versus 670X for Figure 29). None of the etched and corroded samples show the secondary corrosion products evident in the unetched samples.
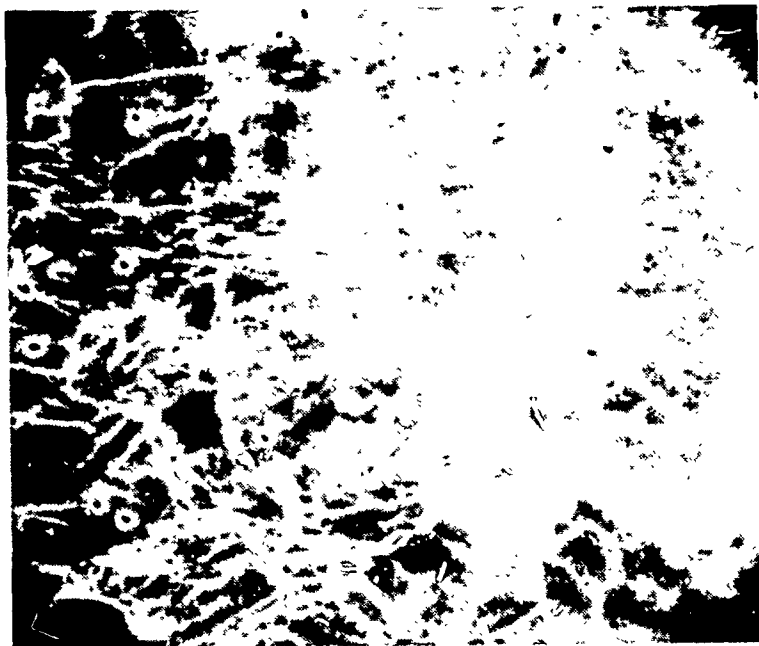
Figure 25

Pre-etched zinc sample showing grain
structure and surface inclusion
distribution, 1260X
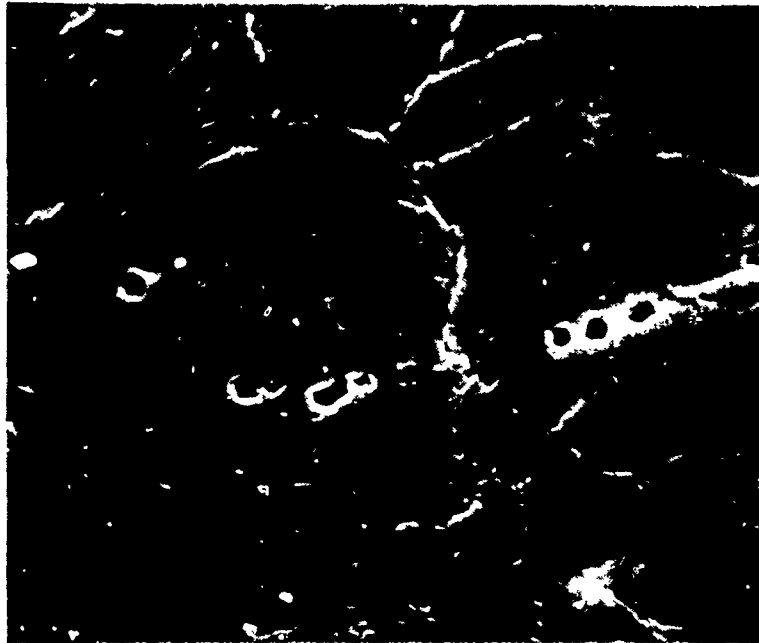
Figure 26

Pre-etched zinc sample showing surface
inclusions and phase transformations
within grains, 2700X
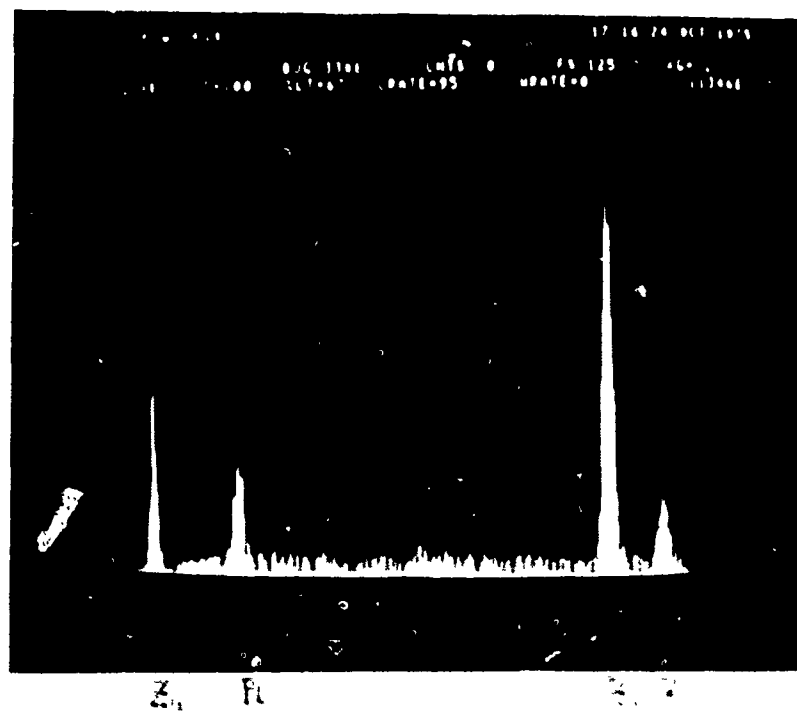
Figure 27

X-ray spectrum of inclusion area on
pre-etched zinc sample showing Zn
and Pb peaks
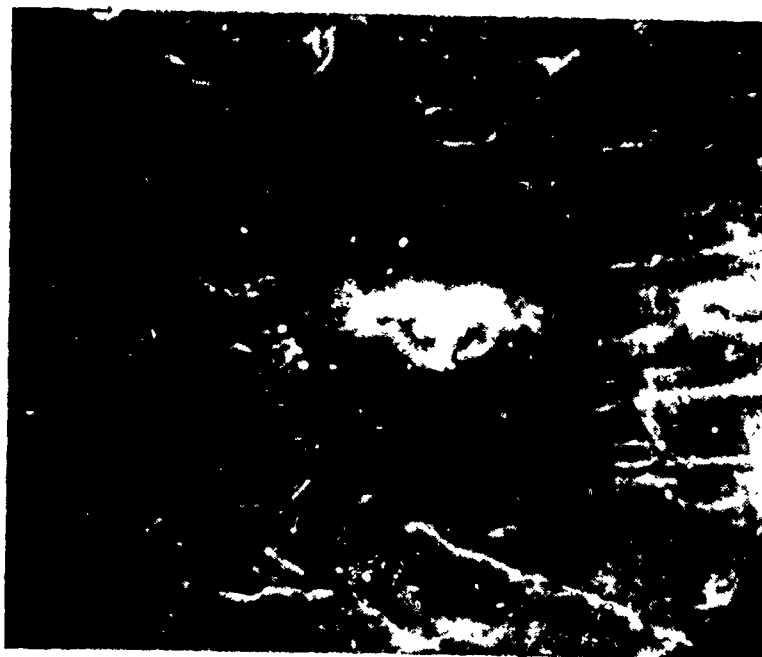
Figure 28

Pre-etched zinc sample with an
atmospheric oxidized inclusion area,
2600X
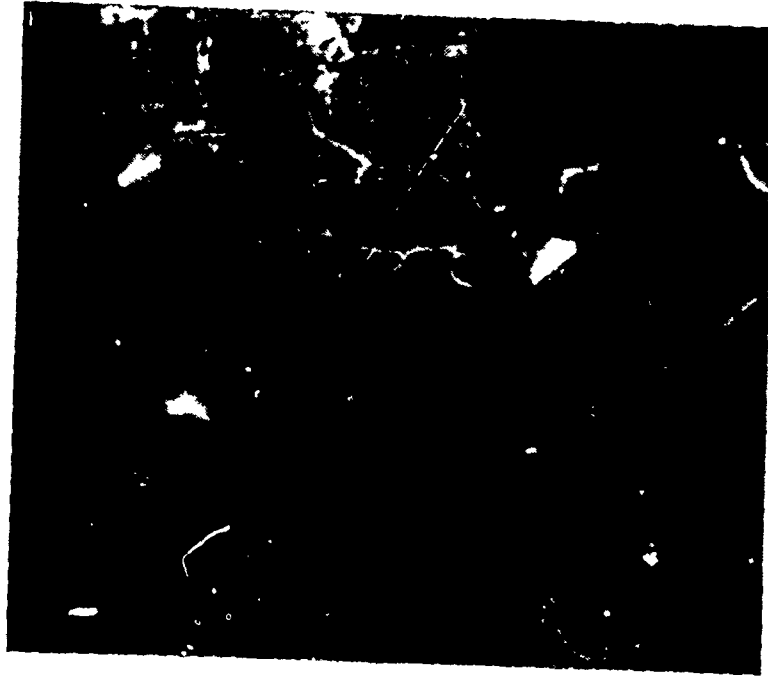
Figure 29

Pre-etched zinc sample, steel couple,
30 minutes exposure, with inclusion
area dissolution, 670X

Figure 30

Pre-etched zinc sample, steel couple,
30 minutes exposure, showing ZnO
platelet growth preferentially at an
inclusion site, 3000X

Figure 31

Pre-etched zinc sample, steel couple,
30 minutes exposure, showing grain
dissolution and ZnO platelet formation,
3000X

Figure 32

Pre-etched zinc sample, steel couple,
30 minutes exposure, showing ZnO
platelet random orientation with respect
to grain structure, 3000X

73

From the evidence illustrated in these microphotographs, grain structure can be concluded to make no contribution to the corrosion process nor does it seem to inhibit or impede the electrochemical dissolution/precipitation mechanism. The "pitted" background zinc is direct photographic evidence of the mechanism of electrochemical dissolution of the base matrix zinc into zinc ions. The "pitting" is uniformly distributed, with a region of lesser attack adjacent to grain boundaries. Figures 33 and 34 are illustrations of this phenomenon and an X-ray analysis spectrum of the grain structure respectively. The inclusion areas are areas of much higher dissolution than the inclusion-free base grains, and the inclusions themselves are microcathodic with respect to the immediate microanodic zinc surrounding them. This accounts for the preferential dissolution at the inclusion areas as is vividly shown in Figure 30. Also of note in this microphotograph is preferred dissolution along the grain boundary. In Figures 31 and 32, it is seen that the hexagonal zinc oxide platelets seem to occur randomly on the surface and are observed to traverse grain boundaries. Figure 35 is a higher magnification view of a platelet traversing a grain boundary, and Figure 36 is the X-ray spectrum of the platelet.
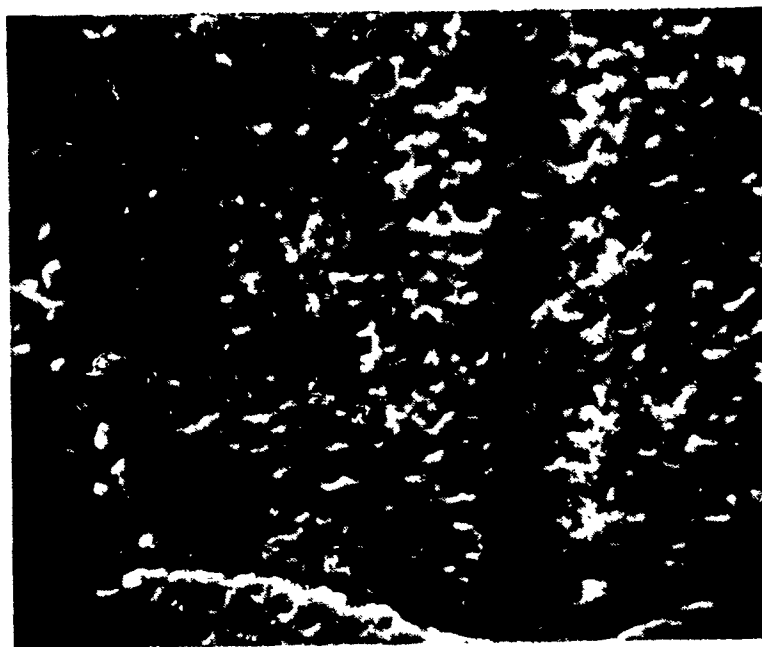
Figure 33

Pre-etched zinc sample, steel coupled,
30 minutes exposure, illustrating the
electrochemical dissolution mechanism
of the base matrix zinc, 6600X

Figure 34

X-ray spectrum of base zinc matrix of
steel coupled, 30 minutes exposure
sample showing only Zn peaks

Figure 35

Pre-etched zinc sample, steel coupled,
30 minutes exposure, illustrating ZnO
platelet traversing a grain boundary,
6600X
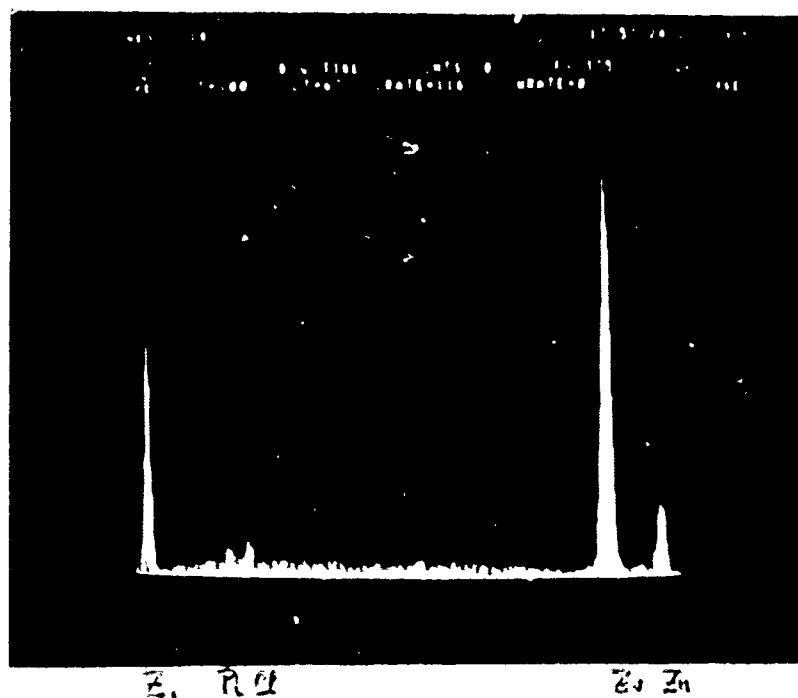
Figure 36

X-ray spectrum of ZnO platelet formed
on the steel coupled, 30 minutes
exposure sample which traverses a
grain boundary

D. X-RAY DIFFRACTION IDENTIFICATION OF CORROSION PRODUCT COMPOUNDS

A Norelco X-ray diffractometer (see Figure 37) was used to qualitatively identify the corrosion products observed in this study. X-ray patterns were run on a number of samples including the time study series discussed previously in Figures 8, 9, 10, 11, 12 and 13 as well as some fifty-minute exposure samples and the passivated sample shown in Figure 23. As a comparison to the clean zinc X-ray pattern, a pattern was run on a sample of commercial "Marz-grade" zinc (99.999% pure). All the results of the X-ray patterns are tabulated in Table III. Another feature of Table III is a tabulation of some of the possible corrosion product patterns which were available in the Hanawalt card deck. This can be used as a comparison to the actual pattern.

ZnO is identified as the major corrosion product from the X-ray patterns. $ZnCO_3$ is found to be a secondary corrosion product. Other compounds which were not specifically identified by the X-ray patterns but known to exist as a result of the X-ray dispersive tests include $Zn(OH)_2$ and a hydrated $ZnCl_2$ compound. Other more complex compounds are probably present but not identifiable from the data base available.

Figure 37

Norelco X-ray Diffractometer

80.

IV. DISCUSSION

A. ELECTROCHEMISTRY OF DISSOLUTION

The introduction of this thesis included a brief dis-
cussion of the electrocher ical nature of corrosion. A more
thorough consideration of the mechanism of zinc anodic
dissolution is now appropriate.

One of the mechanisms proposed for metal dissolution
is the mixed-potential polyelectrode concept. [17] It can
be summarized as follows: There exists on the surface of
the metal which is undergoing dissolution two or more
independent electrode reactions which are related only by
a common electrical potential difference which exists
between the metal and the solution. The emphasis of the
concept is on the currents flowing across the interface and
the potential difference across the interface. Thus in many
cases the existence or the location of separate cathodic and
anodic areas need not be assumed as is usually the case in
the theory of local elements. There is no real distinction,
however, between the mixed potential concept and the theory
of local elements. The latter has been considered a special
case under the former more general theory. It is not necessary

81

to have separate macroscopic areas which are exclusively cathodic or anodic on a metallic surface in order for the dissolution process to proceed by an electrochemical mechanism. Any one site may be anodic during an instant of time and cathodic during another instant, and/or anodic and cathodic processes can occur simultaneously on atomically adjacent sites. The sites also may shift about the surface rapidly during uniform dissolution. The various surface sites may have atomic, microscopic and/or macroscopic dimensions.

In most cases, no given part of a metallic surface is entirely anodic or cathodic on an average time basis unless some special condition exists such as a rectifying film or lack of a necessary reactant at the site in question. In this case, however, nonuniform corrosion under uniform solution conditions does occur so that the dissolution current values of the metal anodes are larger at some surface sites than at others. These differences may arise from variations in composition and structure. Heterogeneities due to composition may supply areas which are predominately cathodic or anodic depending upon the values of the common electrochemical variables of the different reacting systems at the particular sites. Galvanic couples as we have in

this study are a case in point. It has been suggested [17]
that even on an apparent homogeneous surface of a pure metal
the Tafel electrochemical constants for a cathodic reaction
will vary over the surface.

It has been reported [17] that the rate of dissolution
and the reversible potential may differ for the various
crystallographic planes. It is very likely that local
imperfections and zones of disarray (such as edges and
corners of incompletely packed planes, emergent dislocations,
etc.) may be sites of higher activity.

The etching process itself utilizes a dissolution pro-
cess which will pit the surface at dislocation sites if not
properly controlled. For pit formation, the etch rate along
a dislocation must be greater than other etch rates in its
vicinity. The dislocation line has a certain amount of
strain associated with it, even at the surface. In order
to relieve the stress at the surface, it seems logical that
the atoms must rearrange themselves. In doing so, their
bonds become strained, and it is this strain which may
cause nucleation of a pit at a screw dislocation. Also,
dislocations intersecting the surface act as preferred
dissolution sites. It may be possible to correlate ZnO
plate density (number of plates/unit area) with dislocation

density (number of dislocations/unit area). From the evidence found in this study, sea water does in fact play the role of an etchant with initial dissolution on zinc taking place at dislocation sites.

B. CORROSION MODEL

The use of scanning electron microscopy and energy-dispersive X-ray spectroscopy to evaluate anodic mechanisms for zinc is unique to this study. Data developed for steel-coupled zinc samples in sea water electrolyte lead to the following film formation observations:

1. Nucleation of (hexagonally-outlined) ZnO plate-lets on clean coupled surfaces occurs after an incubation time of approximately 10 minutes. The mechanism of oxide platelet nucleation can be postulated to occur within a super-saturated thin layer (about 5 - 10 μm thick) of dissolved zinc ions above the metal surface. The evidence tends to support the hypothesis that the three-dimensional nucleation point is quite close to the base metal surface. In static lab conditions, the zinc-rich ionic boundary layer reaches a steady state concentration level, and the electro-chemical corrosion rate on zinc anodes becomes ion concen-tration polarization dependent. This suggests that if the electrolyte is flowing relative to the anode surface, the

"boundary layer" will become thinner and nucleated ZnO
platelets will tend to be swept away before attaching to
the anode surface.

Velocity effects may cause ZnO platelet precipi-
tation at different orientation angles to the base zinc than
those observed in static tests. Crevice corrosion mechanisms
will also be evident in a fluid situation, and the corrosion
product may change somewhat in crystal morphology. The
corrosion rate will certainly change due to different
polarization values. In fact, flow effects are extremely
important to a full understanding of in-service anode
corrosion characteristics and should be fully investigated.
This variable has not been addressed in the present study.

It is further hypothesized that the hexagonally
shaped oxide platelets grow by lateral extension within the
near surface layer and then settle and attach themselves to
the metal surface with a general preference for orientation
normal to the surface in static circumstances. This is a
favorable (non-passivative) condition. Plates oriented at
high angles to the base metal surface often appear to be
embedded in a field of a fine scale corrosion product.
Figure 38 is a good example of this fine scale base film
product; Figure 39 is the X-ray spectrum, showing Cl and Pb
peaks in addition to Zn.

85

Figure 38

ZnO platelet "buried" in base film
on steel coupled sample, natural sea
water, 25 minutes exposure, 6600X
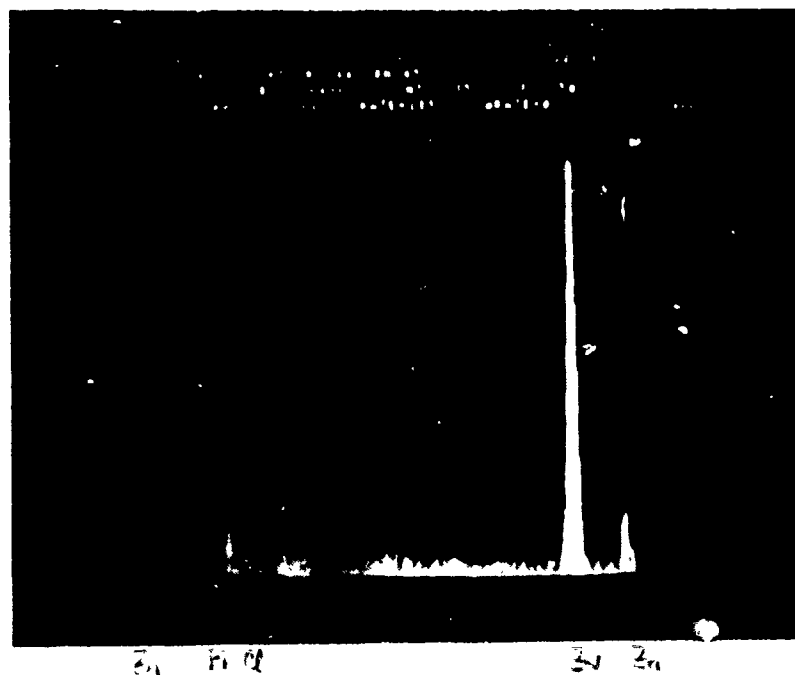
Figure 39

X-ray spectrum for 25 minutes exposure
sample, natural sea water, base film

2. Local surface discontinuities such as surface asperities, scratches and second phase particles (inclusions) in the base metal microstructure form microcells where the corrosion current is initially highest. ZnO plate nucleation is accentuated at asperities and at the periphery of (more cathodic) Fe and Pb-rich inclusion particles. Figures 40 and 41 illustrate initial ZnO plate nucleation at scratches and inclusions respectively.

3. The number of platelets which form as a function of time (nucleation rate) is highly unstable in time exposures from 10 minutes to one hour, in spite of intensive efforts to characterize nucleation frequency. Consequently, data on nucleation rates of ZnO platelets was not tabulated or plotted. The platelets typically form a complete three-dimensional network array after a few hours exposure. In this porous network structure individual plates grow by lateral extension (and some thickening) as further nucleation of plates takes place, leading to an effective thickening of the film network. It was reported earlier [10] that the hexagonal crystal structures grow with the basal (0001) planes parallel to the exposed broad faces of the ZnO crystals, increasing in size by lateral extension, corresponding to growth perpendicular to either the $(11\bar{2}0)$ or $(10\bar{1}0)$ ZnO

88

Figure 40

ZnO platelet initial nucleation site
in a surface scratch on Zn sample, lab
sea water, 5 minutes exposure, 2600X

Figure 41

ZnO platelet initial nucleation site
at inclusion areas on Zn sample, lab
sea water, 10 minutes exposure, 2600X

prism planes. Figures 42 and 43 are representative of the general thickening of the base film.

4. As growth proceeds with time, the size of any given ZnO platelet is found to reach a maximum of about 50 μm diameter, corresponding to a diameter-to-thickness ratio of about 15. As growth of individual plates ceases, nucleation and growth of other plates in the network continue.

An additional feature occasionally seen in lab sea water exposure samples is the formation of local plate clusters as out-croppings above the base film network. As noted earlier for cluster formations at early stages, these groups form over dark-appearing inclusion areas on the anode surface. Figures 24 and 44 are good examples of the cluster growth phenomenon above the base film network.

5. Under appropriate conditions, a passivating phase of film growth occurs consisting of formation of a compact (non-porous) film. This occurs by the formation of a dense secondary level of cluster oxide formation, originating, as mentioned, over "dark" areas on the base zinc surface and leading to platelet formation parallel to the base anode surface, as shown in Figure 23.
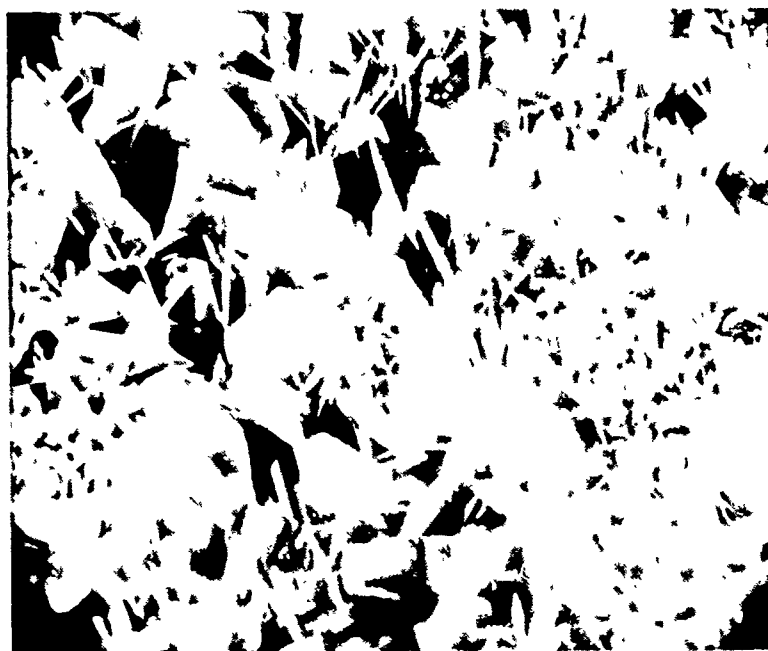
Figure 42

Base film growth on Zn sample, natural
sea water, 51 hours exposure, 284X

Figure 43

Base film growth on Zn sample, natural
sea water, 3 hours exposure, 2600X
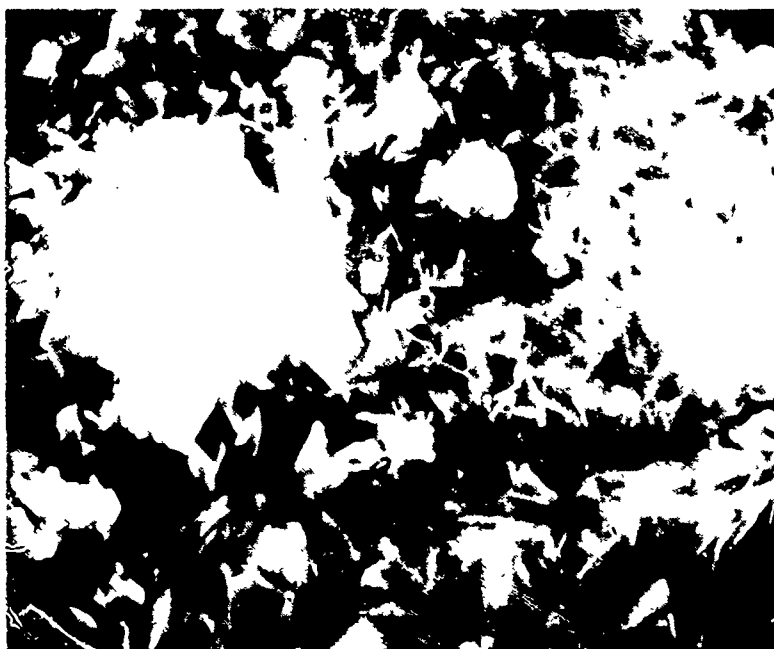
Figure 44

Cluster oxide growth over inclusion
area, lab sea water, 5.5 hours
exposure, 1260X

It is evident in all these observations that base metal impurities have a pronounced effect on corrosion product morphology and distribution in early stage of film growth and that close attention must be paid to the role of specific base metal microstructural features under various electrochemical conditions. Figure 45 schematically illustrates the corrosion film growth model indicated by the observations in this study and detailed above.

C. SECONDARY CORROSION PRODUCTS

Throughout the present observations, products in addition to the hexagonal ZnO plates are in evidence. The most common of these is the "general background film" (see Figure 38) evident in most of the microphotographs seen here. Figure 46 emphasizes the morphology of another product, which may be the same compound as the general background film. The product in Figure 46 has a spongy ball-like appearance and an affinity for attachment to the broad face of the hexagonal platelets. This product could be another morphological form of ZnO or another compound. Figure 47 shows the X-ray spectrum for Figure 42 and has a distinct Cl peak suggesting the possible presence of a zinc chloride ($ZnCl_2$) complex. ($ZnCl_2$ is not crystallographically identified by diffraction.) Figures 46 and 48 illustrate

95
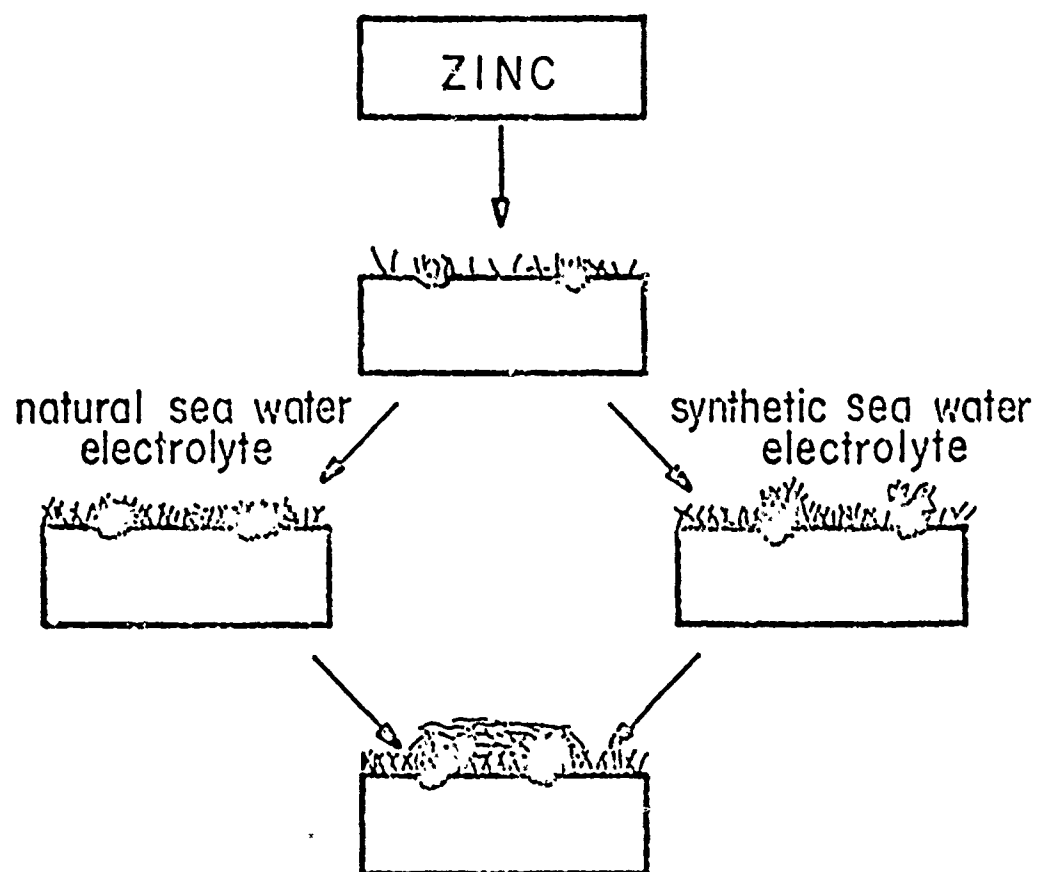
Figure 45

Zinc anode corrosion model

Figure 46

Spongy ball-like secondary corrosion
product growing together over an
oxide cluster on steel coupled zinc,
25 hours exposure, natural sea water,
1300X
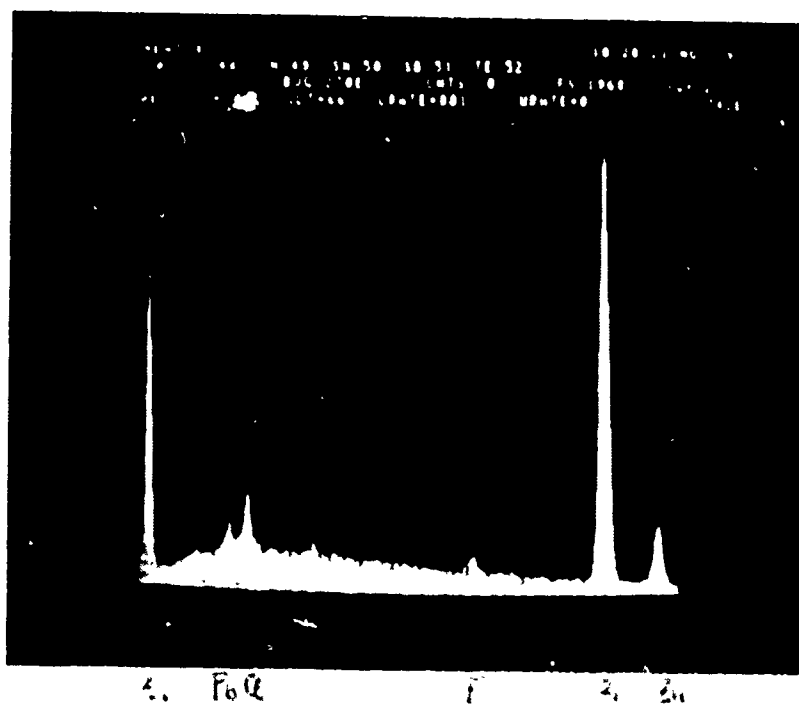
Figure 47

X-ray spectrum of spongy ball-like
corrosion product on steel coupled
zinc, 25 hours exposure

Figure 48

Spongy product filling gaps between
ZnO platelets on steel coupled zinc,
lab sea water, 65 hours exposure,
2600X

that the spongy product tends to grow and fill gaps in the hexagonal ZnO plate network and thus may play a significant role in the growth of a coherent passivating film.

Other corrosion products are evident in small trace amounts on the immersed samples and are presented here in order to catalogue more thoroughly the morphological forms of electrocrystallized products which result from zinc anode corrosion in sea water solution. Figure 49 shows the morphology of a corrosion product unique to specific inclusion areas of a pre-polished and etched sample. This particular form is apparently due to atmospheric oxidation.

Figure 50 is the X-ray spectrum of the product in Figure 45 and shows iron and lead peaks. Figure 51 is another example of the cluster growth phenomenon over the base film. Figure 52 is the X-ray spectrum for the cluster itself (and possibly the underlying volume). It is significant to note that all spectra taken from examples of cluster growth yielded the same relative strengths for the lead and chlorine peaks that are observed in Figure 52. Since lead was observed only at inclusion areas, it can be concluded that the lead in the inclusion areas plays a leading role in the passivating film growth process.

Figure 53 illustrates the morphology of another distinct crystalline corrosion product, determined to contain

Figure 49

Pre-etched zinc showing an atmospheric
oxidized inclusion area, 6600X

Figure 50

X-ray spectrum of atmospheric oxidized
inclusion area showing Zn, Pb and Fe
peaks
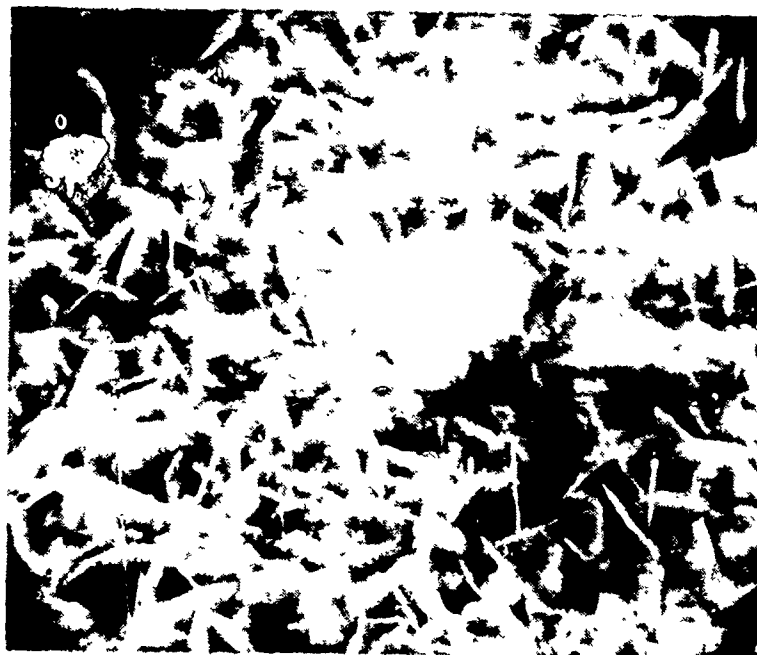
Figure 51

Cluster growth over base film on steel
coupled zinc, natural sea water at $50^{o}C$,
10 minutes exposure, 2570X
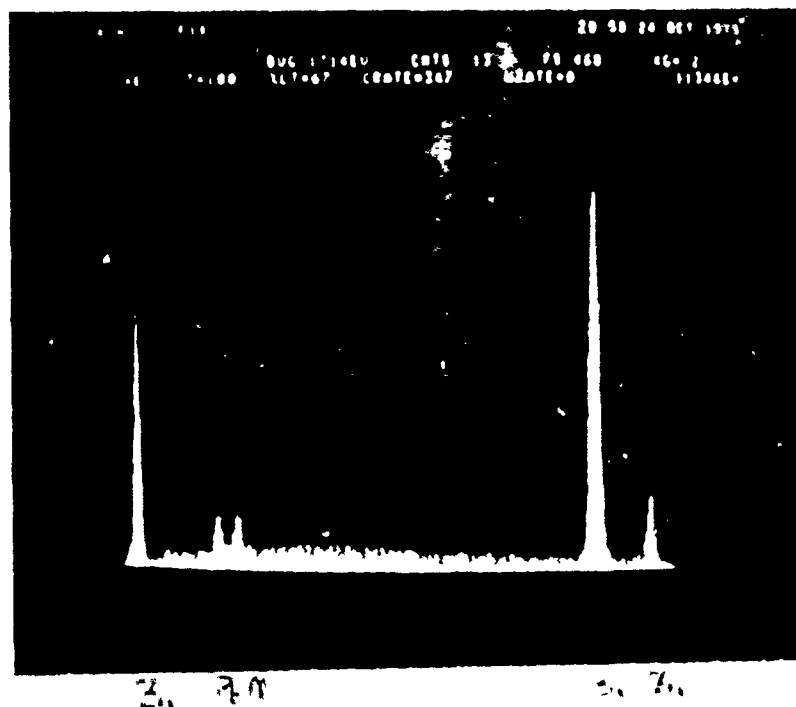
Figure 52

X-ray spectrum of cluster growth and possible underlying volume on steel coupled zinc, natural sea water at 50°C, 10 minutes exposure, showing Zn, Pb, and Cl peaks

Figure 53

Silicon-rich corrosion product on pre-
etched zinc, steel coupled, 30 minutes
exposure, natural sea water, 6300X

proportions of silicon, cadmium, and aluminum. Figure 54
is the spectrum for that product. Figure 55 is a micro-
photograph of another corrosion product type seen on natural
sea water coupled samples. It is of the same morphological
form as the product seen previously in Figure 53, but in
this case the product is formed at the edge of an inclusion
area. The X-ray spectrum (Figure 56) shows some differences
from that corresponding to Figu· ∶ 53, but again with distinc-
tive elemental peaks for silicon, aluminum, lead, cadmium,
iron, and chlorine.

It would appear that the more important secondary
corrosion products are those containing iron and lead.
Etched samples were most useful to study these products
with gross surface irregularities removed, inclusion ar⸱
were more prominent as areas of electrochemical dissolution.
As mentioned, inclusion areas were found to be primarily
lead with traces of iron. Figure 57 shows the corrosion
product at an inclusion area after thirty minute immersion.
This product was found to be iron-rich. The X-ray spectrum
is shown in Figure 58. Figure 59 (spectrum in Figure 60) is
an iron-rich product of the same form as that shown in
Figure 57. This particular form of iron-rich corrosion
product correlates with that seen on unetched coupled samples
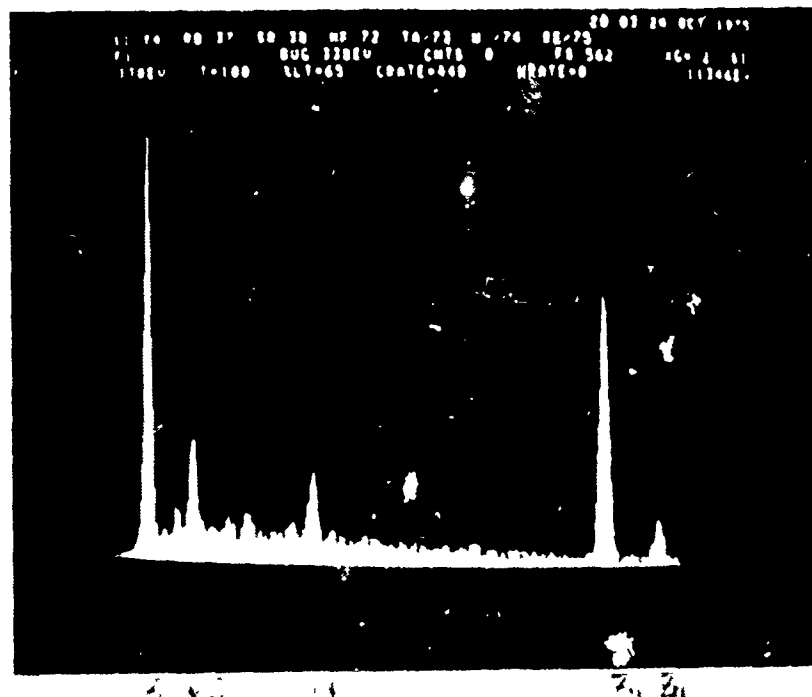
Figure 54

X-ray spectrum of silicon-rich
corrosion product on pre-etched zinc,
30 minutes exposure, natural sea water,
Zn, Si, Al, and Cd peaks showing

107

Figure 55

Silicon-rich corrosion product around
inclusion area on steel coupled zinc
in natural sea water at 50°C, 3 minutes
exposure, 6400X
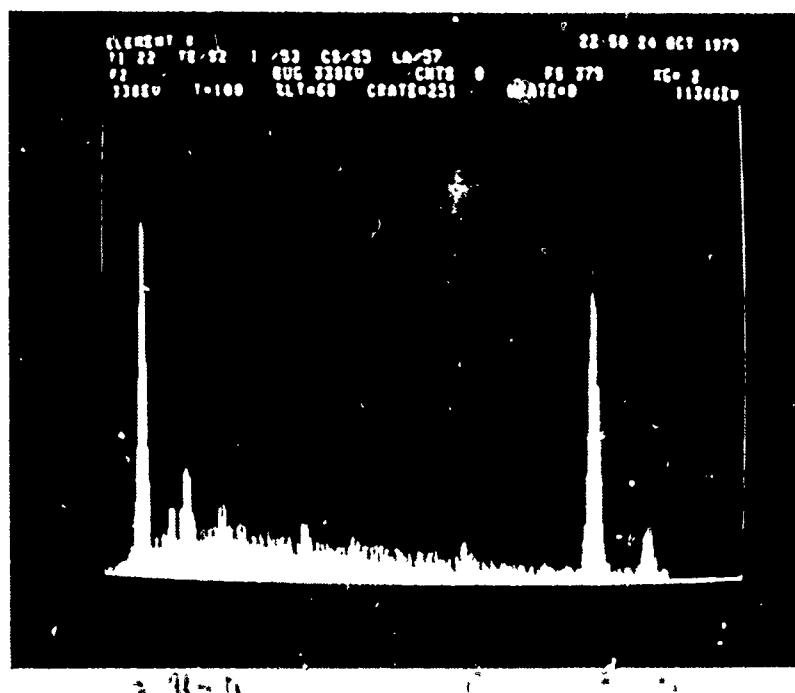
Figure 56

X-ray spectrum of silicon-rich
corrosion product on steel coupled
zinc, 3 minutes exposure, natural
sea water at 50°C, showing Zn, Si, Al,
Fe, Pb, Cd, and Cl peaks

Figure 57

Iron-rich corrosion product on pre-
etched zinc, steel coupled, 30 minutes
exposure, natural sea water, 2550X
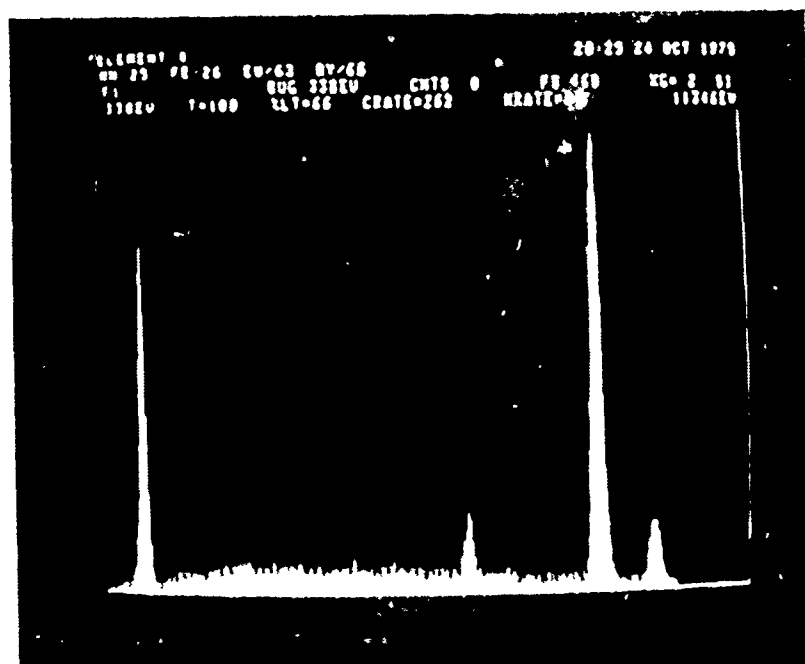
Figure 58

X-ray spectrum of iron-rich corrosion
product on pre-etched zinc, steel
coupled, 30 minutes exposure, natural
sea water, showing Zn and Fe peaks

Figure 59

Iron-rich corrosion product representative of iron product morphology on zinc anodes in natural sea water, 2600X
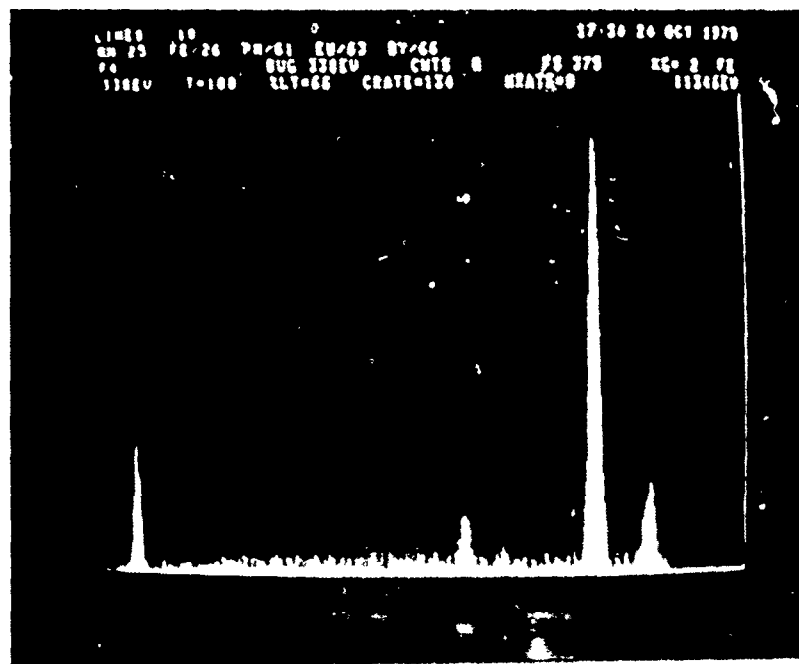
Figure 60

X-ray spectrum of iron-rich corrosion
product showing Zn and Fe peaks

immersed in sea water electrolyte, which showed similar iron product traces of the same crystal morphology. These iron-rich products were not numerous, which is an important observation. Figure 61 shows the affinity of an iron-rich product for attachment to the broad face of a ZnO platelet formation. Lead-rich products found on various samples were more numerous than any other secondary corrosion product and apparently quite important with respect to passivating film formations. Figure 63 illustrates a lead-rich corrosion product under a cluster formation (on an unetched coupled sample). It is interesting to note that the ZnO platelet orientation around this lead-rich formation shows a greater tendency to orient with broad faces parallel to the base zinc surface. Figure 64 is the X-ray spectrum for the lead corrosion product in Figure 63 and shows lead, chlorine and silicon. Figure 65 is another microphotograph of an etched sample inclusion area which has been coupled and immersed for thirty minutes. This particular micro-photograph emphasizes the microcell nature of the process near inclusions. The inclusion is obviously microcathodic with respect to the microanodic zinc surrounding it. When the anodic zinc dissolves, a corrosion product (probably a ZnO product) is precipitated in the ever growing void

114

Figure 61

Iron-rich corrosion product attached
to broad face of ZnO platelet, pre-
etched zinc, steel coupled, 30 minutes
exposure, natural sea water, 2600X
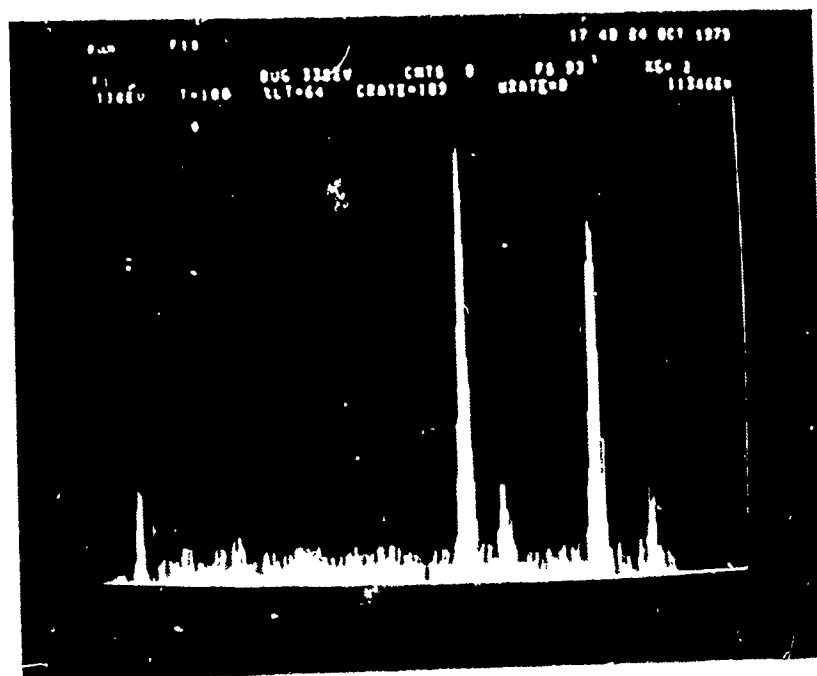
Figure 62

X-ray spectrum of iron-rich corrosion
product attached to broad face of ZnO
platelet, showing Zn and Fe peaks

Figure 63

Lead-rich corrosion product morphology
of steel coupled zinc, 65 hours
exposure, natural sea water, 2600X

Figure 64

X-ray spectrum of long time exposure
lead-rich corrosion product showing
Zn, Pb, Cl, and Si peaks
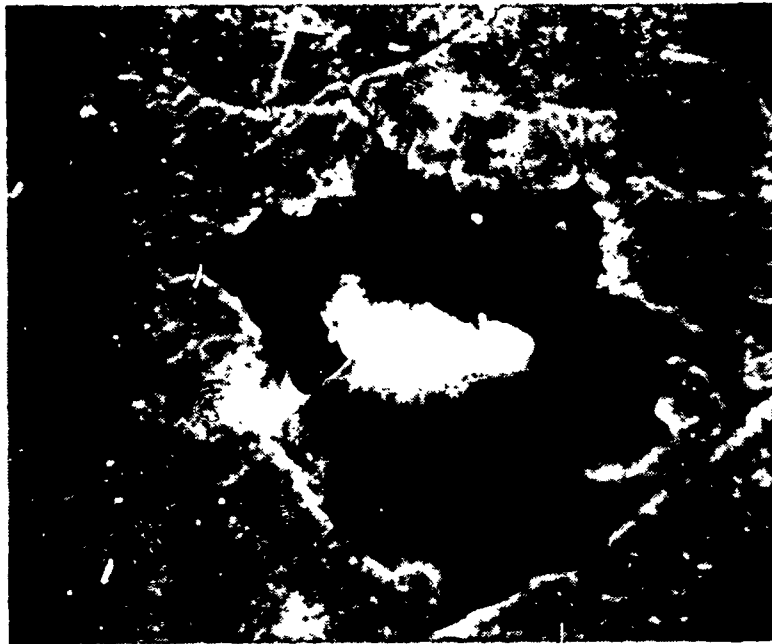
Figure 65

Lead and iron corrosion product in
dissolved inclusion area on pre-
etched zinc, steel coupled, 30
minutes exposure, natural sea water,
2550X

around the inclusion. Figure 65 seems to indicate that this process continues until the zinc dissolves to the extent that the inclusion becomes isolated from the base metal, whereupon it undergoes its own oxidation process. Figure 66 is the X-ray spectrum for the corrosion product discussed above, and it shows lead, chlorine, iron and chromium. Chromium is probably present here as a by-product of the etching process which utilizes chromic acid (see Appendix C). Chromium peaks were eliminated in subsequent samples by a more thorough rinsing process as discussed in the experimental section of this thesis without any resultant change in the corrosion product.

Figure 67 is a mircophotograph of another product of a somewhat different crystal morphology than the previous lead products; Figure 68 shows lead and chlorine peaks for this product. Figure 69 and 71 are examples of the more common form of predominantly lead-rich corrosion product which was found on etched samples after coupling and immersion in sea water electrolyte. Figures 70 and 72 are the X-ray spectrums for Figures 69 and 71 respectively. In Figure 69, the lead product seems to be simply sitting on top of the zinc background rather than at the center such as in Figure 71. The difference in the morphological forms is due to the amount
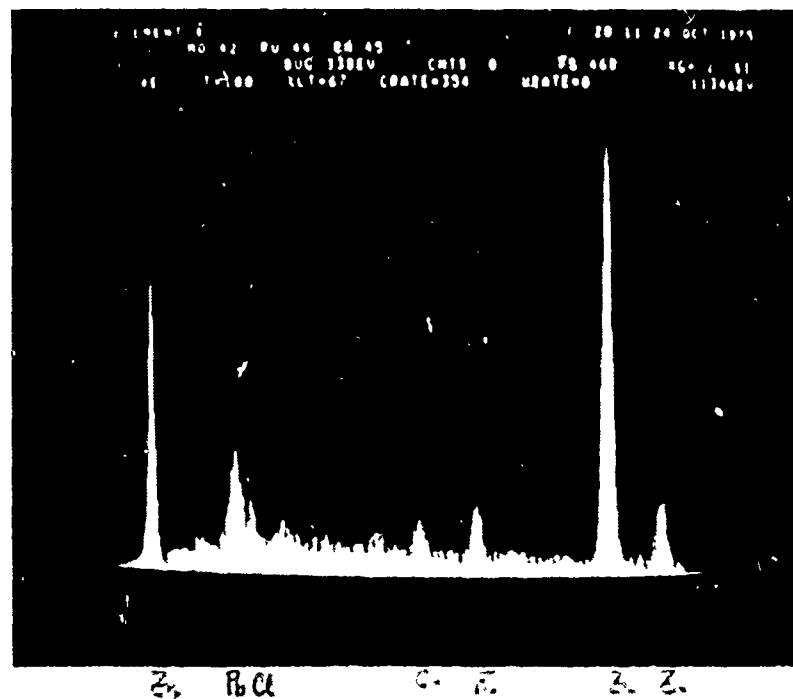
Figure 66

X-ray spectrum of lead and iron
corrosion product showing Zn, Pb,
Fe, Cr, and Cl peaks
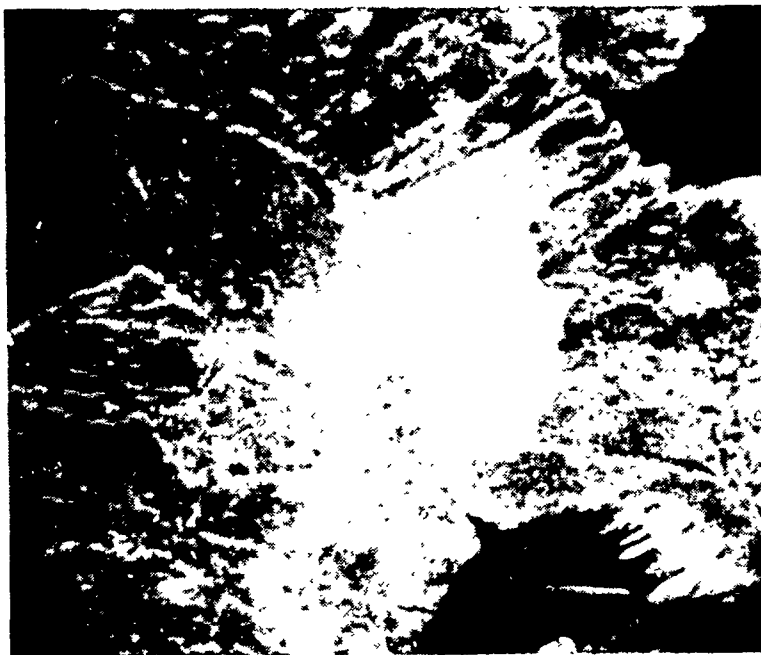
Figure 67

Lead-rich crystal morphology for pre-
etched zinc, steel coupled, 30 minutes
exposure, natural sea water, 2550X
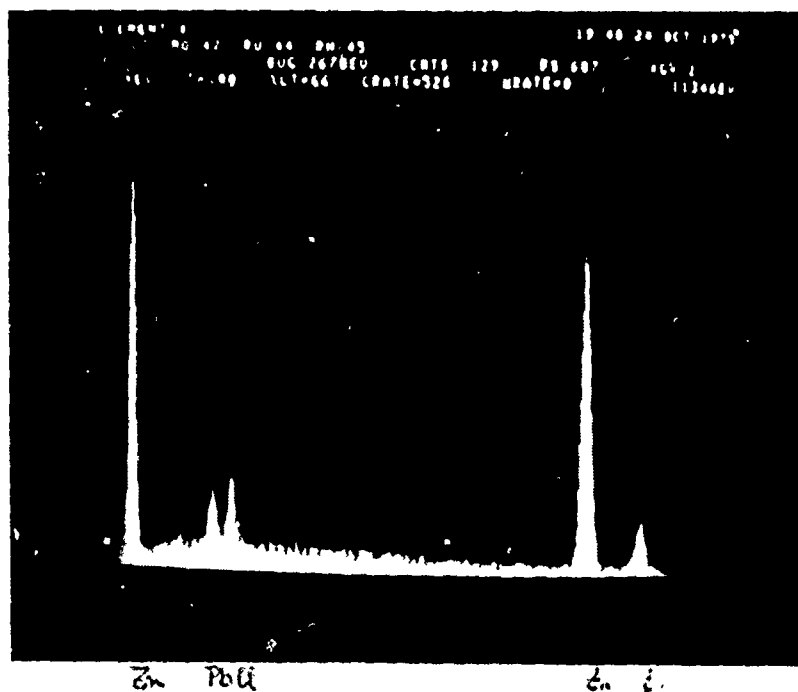
Figure 68

X-ray spectrum of lead-rich crystal
morphology corrosion product showing
Zn, Pb, and Cl peaks

123

Figure 69

Example of lead-rich corrosion product
not in an inclusion area on pre-etched
zinc, steel coupled, natural sea water,
30 minutes exposure, 2550X

Figure 70

X-ray spectrum of lead-rich corrosion
product on base zinc matrix showing
Zn, Pb, and Cr peaks

125
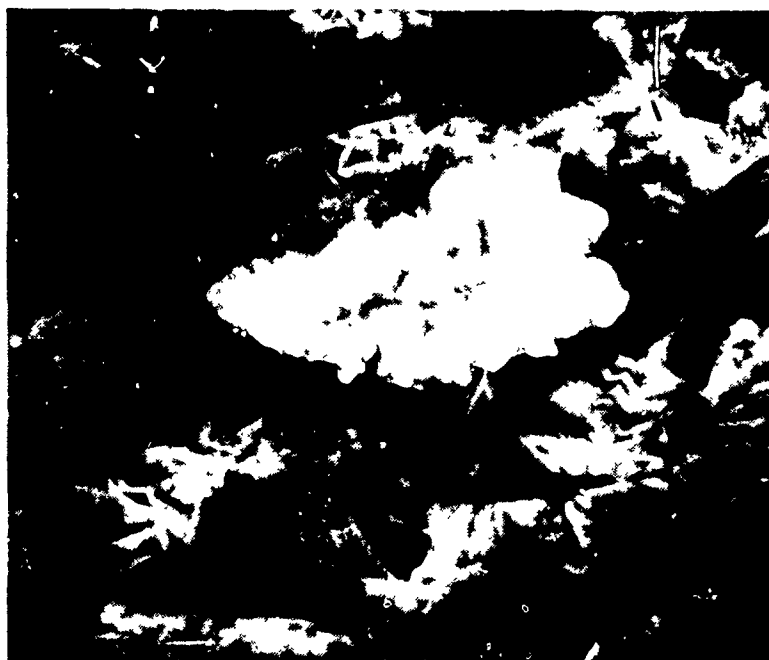
Figure 71

Lead and chromium-rich corrosion
product in an inclusion area on pre-
etched steel coupled zinc, 30 minutes
exposure, natural sea water, 2600X
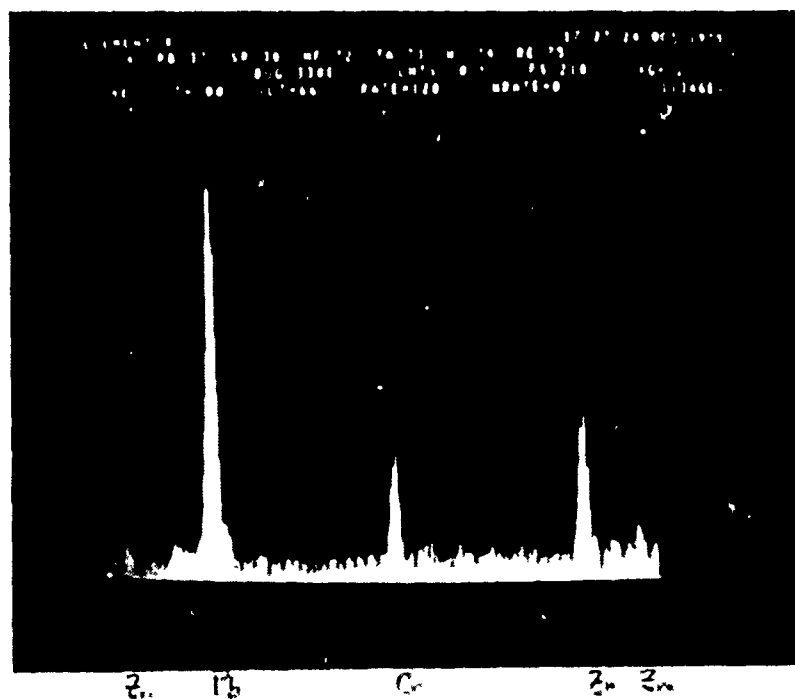
Figure 72

X-ray spectrum of lead and chromium-
rich corrosion product in an inclusion
area showing Zn, Pb, and Cr peaks

of chromium left from the chromic acid etch solution with Figure 71 showing the effect of more chromium. Also, iron and lead-rich corrosion products have been observed to be simply sitting on the base zinc matrix as in Figure 69 on unetched zinc samples, and this could be due to a breaking away and resettling of some particulate during the immersion and rinsing process.

D. CRYSTAL GROWTH

Throughout this thesis there have been numerous references to preferred crystal growth directions for the ZnO corrosion product. The various microphotographs presented show nearly all ZnO platelets attached to the zinc surface at angles in the range of 75° - 115° from the horizontal surface. The reason that randomly nucleated hexagonal shaped crystals have a preferred near normal attachment aspect to the base zinc surface during the precipitation phase of the corrosion mechanism is not clear. An explanation of this phenomenon may involve the well-known electrical double layer theory. [18] The electrical double layer theory postulates that at any metal/electolyte interface, a double layer of opposite ionic charge exists. Any reaction that occurs at the interface is therefore influenced by the electric charges and resulting field produced. In our case,

128

it is apparent that the electric field is normal to the zinc surface and that the ZnO platelets precipitate to the zinc surface at a normal angle. On the other hand, this is not always the case. Some platelets are typically observed to nucleate and grow to full hexagonal shape and precipitate parallel to the surface. Figures 73 and 74 are illustrative examples of parallel platelet precipitation during different phases of the corrosion process.

The ZnO platelets have several distinct morphological forms. The most common is the simple hexagonal crystal shape with blunt edges and with generally not all sides of the hexagon visible above the base film (see Figure 38). A morphological variation is shown in Figure 75. This form has a partial-platelet located near the center of a full platelet, possibly having nucleated at some defect in the full platelet and having a fan shape appearance. This particular feature may be important relative to mechanisms of base film growth during later stages of the corrosion process. In Figure 24, which shows an example of the appearance of a passivating film, platelets grow in a stacking process with a predominance of morphological features such as described above. Another common feature in platelet morphology is shown in Figures 44 and 76 where
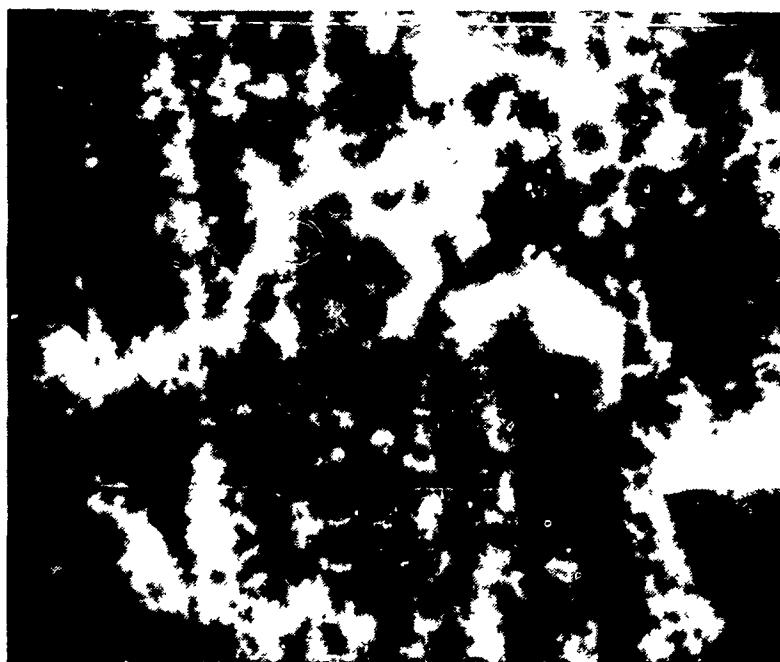
Figure 73

Parallel ZnO platelet growth on steel
coupled zinc, 12 minutes exposure, lab
sea water, 6600X

Figure 74

Parallel ZnO platelet growth over base
film on steel coupled zinc, 50 minutes
exposure, lab sea water, 2650X
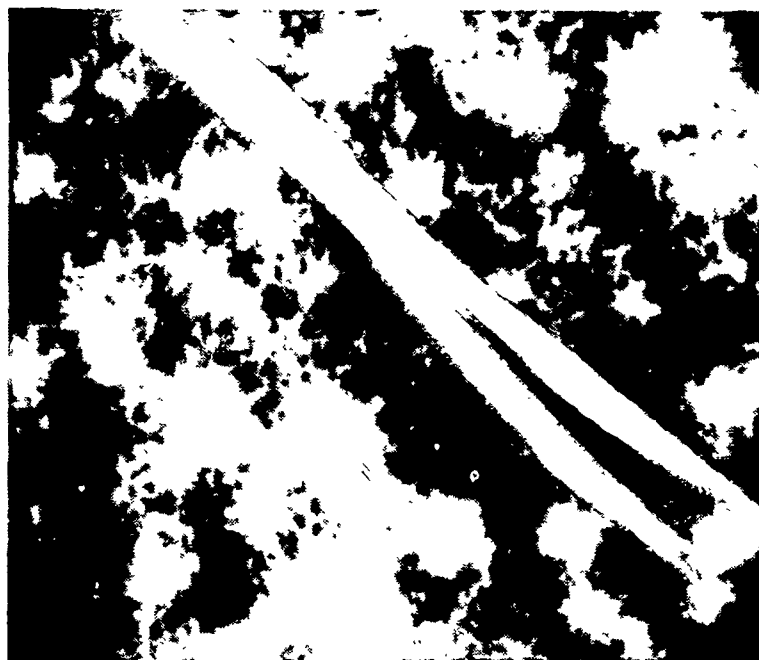
Figure 75

Common ZnO platelet morphology on
steel coupled zinc, 15 minutes
exposure, lab sea water, 6250X

Figure 76

"X" platelet morphology in cluster
formations over base film on steel
coupled zinc, 25 hours exposure,
natural sea water, 250X

133

multiple platelets are attached at a near-normal angle with what must be commonly shared atomic sites. This form is found more often in the cluster oxide formations above inclusion sites.

E. PASSIVATION

Little can be found in the literature which describes the microscopic electrochemical kinetics of passivation effects. Conway [18], in the only thorough discussion that was found of this important aspect of anode performance, has suggested that passivation effects can arise in two or three distinguishable ways: (1) reduction of the available anode surface area for the electrochemical reaction by formation of a corrosion product (generally an oxide or hydroxide); (2) change in the electrochemical standard free energy of activation due to the presence of a corrosion product which changes the energy of activation; (3) change of the catalytic properties and local field at the metal surface by even small surface coverage of corrosion product. The effect (3) is analogous to that considered under (2) but may be more specific and operate at lower surface coverage by corrosion product.

Since the nucleation and growth process slows with time, the surface area reduction effect described above is an

134

obvious contributor to a final passivating film formation.
However, that effect does not cause passivation. Passiva-
tion is found in this study to occur as a result of surface-
parallel ZnO platelet growth such that the electrolyte is
effectively isolated from the zinc surface. Since all the
evidence discussed previously points to inclusion areas as
initiation points for parallel ZnO growth, the effect
described above concerning a local field change is probably
the cause of this phenomenon. The possible local field
change at an inclusion area is shown in Figure 77 below:
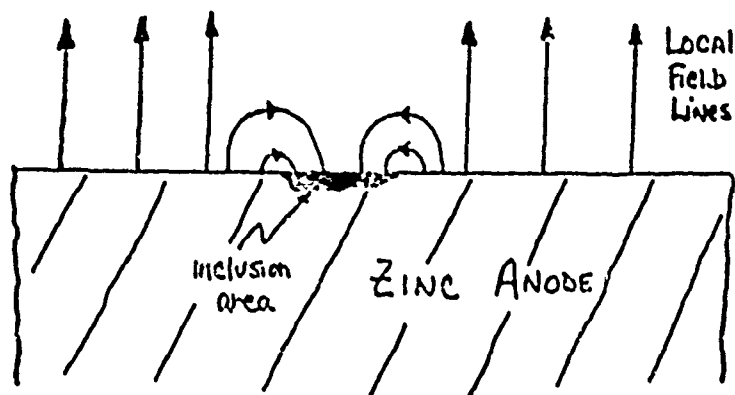
Figure 77

Zinc surface with electric field
lines and the affect of inclusion
areas on the near surface electric
field

The change in the field lines is due to dissimilar metal effects on a microscopic level much the same way an electric field exists macroscopically between the zinc and steel galvanic couple. This causes the platelets to orient with the field lines and precipitate parallel to the zinc surface. Another more obvious effect at inclusion areas is a higher concentration of zinc ions surrounding these areas causing higher local nucleation of the ZnO platelets and subsequent denser oxide film growth.

V. CONCLUSIONS

The following is a list of the significant conclusions reached as a result of this study:

1. Zinc anodes in static sea water conditions corrode according to the model shown in Figure 41 and described in the corrosion model section.

2. Areas near cathodic inclusions on the zinc anode surface are initiation sites for enhanced electrochemical dissolution and are also sites at which passivating film growth tends to begin.

3. Inclusion areas on the U.S. Navy service zinc anodes tested are predominantly lead-rich.

4. Total elimination of elemental impurities is not necessarily the answer to eliminating inclusion area effects, as high purity zinc does not corrode uniformly. Control of the number, distribution, and composition of inclusions in an optimized alloy composition is the most rational approach.

5. The adverse effect of iron with regard to passivation is not evidenced in this study. Therefore, if iron content is kept below the 0.0014% value prescribed by MIL-18001H, it will not be a problem in service.

137

6. In general, present MIL-18001H zinc anodes are only suspect for use on ships which are in port for sustained periods of time. Velocity effects are anticipated to diminish greatly the probability that a passivating film will grow on ships which are underway.

VI. SUMMARY AND RECOMMENDATIONS FOR FURTHER WORK

The efforts to date have concentrated on the mechanisms and kinetics of anodic corrosion product growth on zinc anodes such as are used for cathodic protection applications. The results of this study could be extended by further isolation of individual variables which have been found to have the greatest effect on zinc corrosion behavior. These might include:

1. A determination of the effect of base metal compositional and microstructural variables on macroscopic corrosion rates, corrosion product structures, and nucleation and growth mechanisms. These variables might include grain size effects, phase distribution effects, and alloying element distribution effects.

2. A determination of the effect of electrolyte agitation and velocity on corrosion product structures in order to understand the effect of hydrodynamic disturbances to near-surface electrolyte layers and to the microscopic dissolution-precipitation reactions occurring within.

3. A determination of the effect of potential/ current density variations on corrosion product structures.

4. A determination of the effect of the primary electrochemical variables including temperature, pressure, and dissolved oxygen on corrosion product morphology.

5. Parallel studies of other protective anode alloy systems including aluminum alloys.

A detailed understanding of all the variable effects discussed above ultimately will lead to a better general knowledge of the corrosion process in microscopic detail and will lead to an optimum anode alloy for use in ship hull cathodic protection system.

It is further recommended that natural sea water or its laboratory prepared equivalent be used as the electrolyte in all the above studies in order to simulate more closely in-service conditions.

TABLE I

CHEMICAL ANALYSIS OF ZINC SAMPLES*

Metal	Per Cent Composition
Lead	0.0020
Iron	0.0020
Cadmium	0.0030
Copper	0.0003
Aluminum	0.0010
Silicon	0.0010
Zinc	Remainder

*Spectrographic analysis by Metallurgical Labs, Inc.,
San Francisco, California

TABLE II*

CHEMICAL COMPOSITION OF SYNTHETIC OCEAN WATER
ASTM D 1141

Compound	Concentration, g/liter
NaCl	24.53
$MgCl_2$	5.20
Na_2SO_4	4.09
$CaCl_2$	1.16
KCl	0.695
$NaHCO_3$	0.201
KBr	0.101
H_3BO_3	0.027
$SrCl_2$	0.025
NaF	0.003
$Ba(NO_3)_2$	0.0000994
$Mn(NO_3)_2$	0.0000340
$Cu(NO_3)_2$	0.0000308
$Zn(NO_3)_2$	0.0000096
$Pb(NO_3)_2$	0.0000066
$AgNO_3$	0.00000049

pH concentration after adjustment is 8.2

*see Appendix A

TABLE III

X-RAY POWDER PATTERNS OF SELECTED SAMPLES

Marz Grade (99.999%) Zinc				Clean Zinc			
2θ	$d(A^o)$	I	I/I_1Zn	2θ	$d(A^o)$	I	I/I_1Zn
17.95	4.9377	13	2	36.35	2.4695	470	47
32.75	2.7323	40	5	39.05	2.3048	380	38
36.4	2.4663	760	100	43.25	2.0902	1000	100
39.0	2.3076	55	7	54.4	1.6852	245	25
43.25	2.0902	100+	13	54.5	1.6823	140	14
43.4	2.0833	86	11	70.15	1.3405	210	21
46.15	1.9654	20	3	70.3	1.3380	150	15
54.35	1.6866	38	5	70.65	1.3322	90	9
54.5	1.6823	25	3	70.85	1.3289	88	9
70.1	1.3413	32	4	77.10	1.2360	28	3
70.3	1.3380	19	2	77.25	1.2340	17	2
77.2	1.2347	190	25	82.1	1.1730	165	17
82.1	1.1730	110	14	82.35	1.1700	89	9
82.35	1.1700	67	9	83.75	1.1540	27	3
89.95	1.0898	26	3	86.55	1.1237	101	10
90.25	1.0870	17	2	86.85	1.1206	57	6
115.8	.9093	44	6	90.0	1.0894	29	3
116.25	.9071	27	4	90.3	1.0865	19	2
128.5	.8552	34	4	94.9	1.0456	33	3
129.05	.8533	24	3	95.2	1.0431	24	2
139.2	.8218	100+	13	109.15	.9453	52	5
140.0	.8197	79	10	109.55	.9430	30	3
				115.85	.9091	30	3
				116.4	.9063	56	6
				116.85	.9042	32	3
				124.0	.8724	24.0	2
				124.6	.8700	18	2
				127.45	.8591	73	7
				128.05	.8569	46	5
				131.9	.8435	19	2

Zinc Coupled with Steel in Natural Sea Water Electrolyte, 10-Minute Exposure. (Sample No. 59)

2θ	$d(A^{\circ})$	I	$I/I_1 Zn$	$I/I_1 ZnO$
35.3	2.5406	13.5	1	54
36.3	2.4728	420	42	
37.8	2.3781	13	1	
38.05	2.3630	14	1	
39.15	2.2991	320	32	
39.9	2.2576	14	1	
41.8	2.1593	16	2	
43.3	2.0879	1000	100	
44.65	2.0279	19	2	
54.5	1.6823	172	17	
70.25	1.3388	170	17	
70.37	1.3368	92	9	
70.75	1.3306	130	13	
70.95	1.3273	69	7	
77.20	1.2347	25	3	100
77.40	1.2320	21	2	
82.20	1.1718	131	13	
82.4	1.1694	73	7	
83.8	1.1534	25.5	3	
84.1	1.1501	19	2	
86.62	1.1230	98	10	
86.90	1.1201	51.5	5	
90.05	1.0889	27	3	
90.30	1.0865	19	2	
94.95	1.0452	28	3	
95.25	1.0427	21	2	84
109.2	.9450	41	4	
109.6	.9427	25	3	
115.95	.9086	29	3	
116.5	.9059	49	5	100+
116.95	.9037	27.5	3	
124.05	.8722	22	2	
124.6	.8700	15.5	2	
127.5	.8589	72	7	
128.1	.8567	47	5	

Zinc Coupled with Steel in Natural Sea Water Electrolyte, 12-Minute Exposure. (Sample No. 60)

2θ	d(A°)	I	I/I₁Zn	I/I₁ZnO
35.3	2.5406	13	2	$\underline{50}$
36.3	2.4728	312	$\underline{48}$	
37.7	2.3842	12.5	2	
39.2	2.2963	180	$\underline{27}$	
39.95	2.2549	12	2	
42.0	2.1495	14	2	
43.2	2.0925	655	$\underline{100}$	
44.65	2.0279	16	2	
54.55	1.6809	94	$\underline{14}$	
70.3	1.3380	101	$\underline{15}$	
70.85	1.3289	74	$\underline{11}$	
77.25	1.2340	26	$\underline{4}$	$\underline{100}$
82.25	1.1712	72	$\underline{11}$	
82.50	1.1683	50	8	
83.9	1.1523	17	$\underline{3}$	
84.0	1.1512	17	3	
86.7	1.1221	61	$\underline{9}$	
86.95	1.1196	33	5	
90.15	1.0879	21	$\underline{3}$	
90.4	1.0856	15		
95.0	1.0448	21.5	$\underline{3}$	
95.4	1.0415	12	2	$\underline{46}$
109.25	.9447	33	$\underline{5}$	
109.7	.9421	20.5	3	
115.95	.9086	38	$\underline{6}$	
116.50	.9059	50.5	8	$\underline{100}^+$
116.95	.9036	25.5	4	
124.2	.8716	18	$\underline{3}$	
124.7	.8696	13	2	
127.5	.8589	60	$\underline{9}$	
128.1	.8567	37	6	
132.0	.8432	14	2	

Zinc Coupled with Steel in Natural Sea Water Electrolyte, 15 Minutes Exposure. (Sample No. 61)

2θ	$d(\text{A}^\circ)$	I	$I/I_1 Zn$	$I/I_1 ZnO$
35.3	2.5406	12	1	<u>50</u>
36.5	2.4597	380	<u>40</u>	
39.2	2.2963	280	<u>30</u>	
41.9	2.1544	17.5	2	
43.3	2.0879	940	<u>100</u>	
44.65	2.0279	16	2	
54.5	1.6823	130	<u>14</u>	
70.25	1.3388	130	<u>14</u>	
70.4	1.3363	85	<u>9</u>	
70.75	1.3306	100⁺	<u>11</u>	
71.0	1.3265	65	7	
77.2	1.2347	26	<u>3</u>	<u>100</u>⁺
77.45	1.2313	20	2	
82.2	1.1718	100⁺	<u>11</u>	
82.45	1.1689	64	7	
83.85	1.1529	24	<u>3</u>	
84.15	1.1495	16	2	
86.65	1.1227	86	<u>9</u>	
86.90	1.1201	56	6	
90.1	1.0884	21	<u>2</u>	
90.35	1.0861	15	2	
95.0	1.0448	28	<u>3</u>	<u>63</u>
95.25	1.0427	16.5	2	
109.2	.9450	40	<u>4</u>	
109.65	.9424	26	3	
115.95	.9086	29	<u>3</u>	<u>100</u>⁺
116.5	.9059	47	<u>5</u>	
116.95	.9037	25	3	
124.1	.8720	23	<u>2</u>	
124.65	.8698	17	2	
127.5	.8589	70	<u>7</u>	
128.1	.8567	42	4	
131.95	.8434	15	2	

Zinc Coupled with Steel in Synthetic Sea Water Electrolyte, 15 Minutes Exposure. (Sample No. 80)

2θ	$d(A^\circ)$	I	$I/I_1 Zn$	$I/I_1 ZnO$
36.55	2.4565	580	74	
39.20	2.2963	305	39	
43.45	2.0810	780	100	
54.50	1.6823	120	15	
54.60	1.6795	110	14	
70.3	1.3380	130	17	
70.80	1.3298	77	10	
77.25	1.2340	37	5	100
77.40	1.2320	28	4	
82.25	1.1712	86	11	
82.50	1.1683	58	7	
83.90	1.1523	24	3	
86.70	1.1221	86	11	
86.95	1.1196	53	7	
90.10	1.0884	25	3	
95.05	1.0444	28	4	
95.35	1.0419	18	2	50

Zinc Coupled with Steel in Natural Sea Water Electrolyte,
20 Minutes Exposure.   (Sample No. 62)

2θ	$d(A^O)$	I	$I/I_1 Zn$	$I/I_1 ZnO$
35.3	2.5406	12	1	44
36.45	2.4630	370	37	
39.40	2.2851	260	26	
43.65	2.0720	1000	100	
54.50	1.6823	150	15	
70.25	1.3388	130	13	
70.75	1.3306	100+	10	
77.20	1.2347	27	3	100
82.20	1.1718	100+	10	
82.40	1.1694	76	8	
83.80	1.1534	24	2	
86.65	1.1227	85	8	
86.90	1.1201	48	5	
90.10	1.0884	21	2	
95.00	1.0448	27	3	
95.30	1.0423	17	2	63
109.20	.9450	42	4	
109.65	.9424	27	3	
115.95	.9086	32	3	
116.50	.9059	48	5	100+
116.90	.9039	27	3	
124.10	.8720	19	2	
127.50	.8589	70	7	
128.10	.8567	46	5	
132.95	.8401	17	2	
139.00	.8224	31	3	
139.70	.8205	20	2	

Zinc Coupled with Steel in Lab Sea Water Electrolyte,
20 Minutes Exposure.   (Sample No. 78)

2θ	$d(A^O)$	I	$I/I_1 Zn$	$I/I_1 ZnO$
20.55	4.3185	14	2	
32.85	2.7242	14	2	
33.55	2.6690	13	1	
35.75	2.5096	23	3	50
36.45	2.4630	900	100	
39.15	2.2991	310	34	
43.40	2.0833	890	99	
54.45	1.6838	130	14	
70.20	1.3396	140	16	
70.40	1.3363	98	11	
70.75	1.3306	130	14	
70.95	1.3273	71	8	
77.15	1.2354	54	6	100
82.20	1.1718	100+	11	
82.45	1.1689	59	7	
83.85	1.1529	27	3	
86.60	1.1232	99	11	
86.90	1.1201	57	6	
90.05	1.0889	30	3	
90.30	1.0865	18	2	

Zinc Coupled with Steel in Synthetic Sea Water Electrolyte, 50 Minutes Exposure. (Sample No. 105)

2θ	d(A°)	I	I/I₁Zn	I/I₁ZnO
25.5	3.4903	11	2	
32.9	2.7202	12	2	
33.7	2.6574	12	2	50
36.55	2.4565	230	32	
39.25	2.2935	210	29	
43.45	2.0810	720	100	
54.60	1.6795	92	13	
70.35	1.3372	94	13	
70.80	1.3298	87	12	
77.35	1.2327	22	3	100
82.30	1.1706	83	12	
83.90	1.1523	23	3	
86.75	1.1216	75	10	
86.95	1.1196	50	7	
90.15	1.0879	20	3	

Zinc Coupled with Steel in Lab Sea Water Electrolyte,
50 Minutes Exposure. (Sample No. 106)

2θ	d(A$^{\circ}$)	I	I/I$_1$Zn	I/I$_1$ZnO
35.35	2.5371	13	2	50
36.55	2.4565	260	33	
39.2	2.2963	230	29	
39.95	2.2549	14	2	
42.5	2.1253	20	3	
43.5	2.0788	790	100	
54.6	1.6795	100	13	
70.25	1.3388	100	13	
70.80	1.3298	92	12	
77.25	1.2340	27	3	100
82.3	1.1706	86	11	
82.5	1.1683	53	7	
83.9	1.1529	25	3	
84.1	1.1501	15.5	2	
86.75	1.1216	77	10	
87.0	1.1190	45	6	
90.2	1.0875	20	3	
90.4	1.0856	15	2	
95.0	1.0448	22	3	
95.3	1.0423	17	2	

Zinc Coupled with Steel in Lab Sea Water Electrolyte,
4 Hours Exposure.   (Sample No. 93)

2θ	$d(A^O)$	I	I/I_1Zn	I/I_1ZnO	I/I_1ZnCO_3
20.6	4.3081	15.5	2		
21.45	4.1393	27	4		
24.1	3.6898	17	2		
25.5	3.4903	42	5		100
27.5	3.2408	14	2		
28.4	3.1401	15	2		
29.85	2.9908	14	2		
30.25	2.9522	23	3		
32.4	2.7610	13.5	2	43	32
32.9	2.7202	40	5		
33.6	2.6651	42	5	100+	
35.2	2.5475	15	2		
35.75	2.5096	41	5	100+	
36.5	2.4597	510	67	100+	
37.45	2.3995	21	3		
39.2	2.2963	210	28		
43.4	2.0833	760	100		
48.4	1.8791	18	2	60	
54.5	1.6823	100+	13		
58.5	1.5765	19	2	63	
59.0	1.5643	16	2	53	
60.3	1.5337	11	1		26
62.65	1.4817	12	2	40	
70.25	1.3388	135	18		
70.5	1.3347	77	10		
70.8	1.3298	86	11		
71.0	1.3265	52	7		
77.25	1.2340	30.5	4	100	
77.5	1.2307	22	3	73	
82.25	1.1712	101	13	100+	
82.5	1.1683	60	8		
83.9	1.1523	23	3		
84.2	1.1490	11	1		
86.7	1.1221	74.5	10		
86.9	1.1201	44	6		
90.1	1.0884	24	3		
90.4	1.0856	17	2		
95.05	1.0444	26	3		
95.35	1.0419	15	2		

Zinc Coupled with Steel in Natural Sea Water Electrolyte, 427 Hours Exposure.   (Sample No. 95)

2θ	$d(A^{\circ})$	I	$I/I_1 Zn$	$I/I_1 ZnO$	$I/I_1 ZnCO_3$
13.80	6.4119	97	54		
14.25	6.2104	27	15		
18.50	4.9721	23	13		
20.40	4.3499	65	36		
21.45	4.1393	36	20		
24.05	3.6973	39	22		
25.50	3.4903	69	38		87
27.55	3.2351	62	34		
28.40	3.1401	36	20		
29.85	2.9908	30	17		
30.25	2.9522	67	37		
32.35	2.7652	23	13		
32.95	2.7162	79	44	88	100
33.65	2.6613	86	48	97	
35.10	2.5546	31	17		
35.75	2.5096	90	50	100	
36.60	2.4532	69	38		
37.35	2.4057	34	19		
39.15	2.2991	61	34		77
41.75	2.1618	16	9		
43.45	2.0810	180	100		100+
48.40	1.8791	47	26	52	
49.05	1.8557	22	12		
54.05	1.6953	48	27		61
54.60	1.6795	36	20		
58.50	1.5765	43	24	48	
59.0	1.5643	36	20	40	
60.30	1.5337	30	17		38
62.70	1.4806	18	10	20	23
66.95	1.3966	21	12	23	
69.0	1.3600	17	9	19	
70.30	1.3380	50	28	56	63
70.85	1.3289	27	15	30	
71.05	1.3257	24	13		
77.25	1.2340	16	9	18	
82.30	1.1706	31	17		
86.75	1.1216	27	15		
90.20	1.0875	19	11		

2θ	$d(A^{o})$	I	I/I_1Zn	I/I_1ZnO	I/I_1ZnCO_3
109.25	.9447	18	$\underline{10}$		$\underline{25}$
116.0	.9083	20	$\underline{11}$		
116.50	.9054	29	$\underline{16}$	$\underline{32}$	
117.0	.9034	18	$\overline{10}$		
127.35	.8594	29	$\underline{16}$		
128.20	.8563	19	$\overline{11}$		

TABLE IV

HANAWALT X-RAY POWDER PATTERN STANDARD DATA

Zn			ZnO		
$d(A^O)$	I/I_1	hkl	$d(A^O)$	I/I_1	hkl
2.473	53	002	2.816	71	100
2.308	40	100	2.602	56	002
2.091	100	101	2.476	100	101
1.687	28	102	1.911	29	102
1.342	25	103	1.626	40	110
1.332	21	110	1.477	35	103
1.237	2	004	1.407	6	200
1.1729	23	112	1.379	28	112
1.1538	5	200	1.359	14	201
1.1236	17	201	1.301	3	004
1.0901	3	104	1.238	5	202
1.0456	5	202	1.1812	3	104
0.9454	8	203	1.0920	10	203
0.9093	6	105	1.0639	4	210
0.9064	11	114	1.0422	10	211
0.8722	5	210	1.0158	5	114
0.8589	9	211	0.9848	4	212
0.8437	2	204	0.9764	7	105
0.8245	1	006	0.9555	1	204
0.8225	9	212	0.9382	4	300
			0.9069	12	213
			0.8826	6	302
			0.8675	1	006
			0.8369	6	205
			0.8290	2	106
			0.8237	2	214
			0.8125	5	220

ZnCO$_3$			α - ZnCl$_2$		
d(A^o)	I/I$_1$	hkl	d(A^o)	I/I$_1$	hkl
3.55	49	012	4.79	65	011
2.750	100	104	3.08	100	112
2.329	25	110	2.903	20	013
2.110	18	113	2.351	25	121
1.946	26	202	1.975	16	123
1.776	11	024	1.928	8	015
1.703	44	116,018	1.910	25	220
1.515	13	211	1.866	45	024
1.493	13	122	1.773	6	031
1.411	9	214	1.621	30	132
1.408	2	1.0.10	1.595	6	033
1.374	3	208	1.509	25	125,116
1.357	2	119	1.482	8	231
1.343	9	300	1.423	4	017
1.2524	6	0.0.12	1.374	6	233
1.2423	1	217	1.357	4	035
1.2048	3	0.2.10	1.350	10	040
1.1833	8	306,128	1.299	4	141
1.1632	1	220	1.290	4	008
1.1057	2	312	1.259	4	127
1.1028	2	1.1.12	1.236	6	332
1.0710	6	134	1.225	2	143
1.0699	3	2.1.10	1.212	16	235,136
1.0552	2	226	1.105	2	145
1.0371	<1	0.1.14	1.094	16	244
0.9730	5	404			
0.9606	8	318			
0.9473	1	2.0.14			
0.9201	3	1.1.15			
0.9174	3	232			
0.9160	8	3.0.12			
0.8977	<1	324			
0.8967	<1	1.3.10			
0.8878	<1	048			
0.8793	1	410			
0.8775	<1	1.2.14			
0.8523	1	2.2.12			
0.8514	<1	0.2.16			
0.8370	<1	4.0.10			

β - PbO$_2$			ZnCl$_2$ · 4Zn(OH)$_2$		
d(A^O)	I/I$_1$	hkl	d(A^O)	I/I$_1$	hkl
3.50	100$^+$	110	7.87	100	003
2.79	80	101	5.35	21	101
2.46	90	200	4.02	21	104
1.85	50	211	3.94	8	006
1.75	50	220	3.58	23	105
1.68	50	002	3.17	37	110
1.556	30	310	2.940	31	113
1.519	30	112	2.878	25	107
1.486	50	301	2.725	53	201
1.387	30	202	2.672	67	202
1.273	50	321	2.601	21	108
1.238	30	400	2.488	3	204
1.214	30	222	2.470	10	116
1.152	30	312	2.374	37	205
			2.174	5	1.0.10
			2.067	7	211
			2.023	22	119
			2.012	9	208
			1.971	4	0 0.12
			1.957	9	214
			1.900	8	215
			1.830	4	300
			1.792	8	2.0.10
			1.782	5	303
			1.768	13	217
			1.699	13	218
			1.693	12	2.0.11
			1.674	2	1.1.12
			1.660	3	306
			1.585	36	220
			1.554	15	223
			1.517	14	2.0.13
			1.502	8	309
			1.475	5	314
			1.471	4	226
			1.449	3	315
			1.439	4	2.0.14
			1.388	5	317
			1.369	7	401

TABLE V

ZINC SAMPLE COMPILATION SHEET

(All samples tested at 25°C unless noted)

SAMPLE NO.	ELECTROLYTE	TIME	STEEL COUPLE	SEM	X-RAY
1				X	
2	dist. water	2 min		X	
3	dist. water	5 min		X	
4	dist. water	32 min		X	
5	dist. water	5 hr		X	
6	tap water	24 hr		X	
7	dist. water	24 hr		X	
8	tap water	20 hr		X	
9	dist. water	20 hr		X	
10	nat. sea	2 min		X	
11	nat. sea	5 min		X	
12	nat. sea	32 min		X	
13	nat. sea	12 hr		X	
14	nat. sea	5.75 hr		X	
15	nat. sea	9.5 hr		X	
16	nat. sea	12 hr	X	X	
17	nat. sea	6 hr	X	X	
18	nat. sea	2 min	X	X	
19	nat. sea	5 min	X	X	
20	nat. sea	30 min	X	X	
21	nat. sea	1.5 hr	X	X	
22	nat. sea	16.5 hr	X	X	
23	nat. sea	3 min	X	X	
24	nat. sea	5 min	X	X	
25	nat. sea	7 min	X	X	
26	nat. sea	9 min	X	X	
27	nat. sea	36 min	X	X	
28	nat. sea	2.5 hr	X	X	
29	nat. sea	1.5 hr	X	X	
30	nat. sea	17 hr	X	X	
31	dist. water	17 hr	X	X	
32	dist. water	2.5 hr	X	X	
33	nat. sea	2.5 hr	X	X	
34	nat. sea	1 hr	X	X	
35	dist. water	4.3 hr	X	X	

SAMPLE NO.	ELECTROLYTE	TIME	STEEL COUPLE	SEM	X-RAY
36	nat. sea	4.3 hr	X	X	
37	nat. sea	5.2 hr	X	X	
38	nat. sea	51 hr	X	X	
39	nat. sea	64 hr	X	X	
40				X	X
41	nat. sea	1 min	X	X	
42	nat. sea	2 min	X	X	
43	nat. sea	3 min	X	X	
44	nat. sea	4 min	X	X	
45	nat. sea	5 min	X	X	
46	nat. sea	7 min	X	X	
47	nat. sea	10 min	X		
48	nat. sea	12 min	X		
49	nat. sea	15 min	X		
50	nat. sea	20 min	X		
51	nat. sea	25 min	X	X	
52	nat. sea	30 min	X		
53	nat. sea	1 min	X		
54	nat. sea	2 min	X		
55	nat. sea	3 min	X	X	
56	nat. sea	4 min	X		
57	nat. sea	5 min	X		
58	nat. sea	7 min	X	X	
59	nat. sea	10 min	X	X	X
60	nat. sea	12 min	X	X	X
61	nat. sea	15 min	X	X	X
62	nat. sea	20 min	X	X	X
63	nat. sea	25 min	X	X	
64	nat. sea	30 min	X	X	
65	nat. sea	35 min	X	X	
66	nat. sea	40 min	X	X	
67	0.1 NaCl	20 min	X	X	
68	0.1 NaCl	10 min	X		
69	0.1 NaCl	15 min	X		
70	nat. sea	1.2 hr	X	X	
71	nat. sea	30 min	X	X	
72	nat. sea	20 min	X		
73	nat. sea	22 min	X	X	
74	nat. sea	20 min	X		
75	nat. sea	25 hr	X	X	
76	nat. sea	113 hr	X	X	
77	nat. sea	187 hr	X	X	

SAMPLE NO.	ELECTROLYTE	TIME	STEEL COUPLE	SEM	X-RAY
78	lab sea	18 hr	X	X	X
79	lab sea	20 min	X	X	X
80	lab sea	15 min	X	X	X
81	lab sea	10 min	X	X	
82	lab sea	30 min	X	X	
83	lab sea	40 min	X	X	
84	lab sea	3 hr	X	X	
85	lab sea	17 hr	X	X	
86	lab sea	5 min	X	X	
87	lab sea	7 min	X	X	
88	lab sea	10 min	X	X	
89	lab sea	12 min	X	X	
90	lab sea	15 min	X	X	
91	lab sea	20 min	X	X	
92	lab sea	25 min	X	X	
93	lab sea	4 hr	X	X	X
94	lab sea	1 hr	X	X	
95	nat. sea	427 hr	X	X	X
96	lab sea	24 hr	X	X	
97	lab sea	5.4 hr	X	X	
98	lab sea	12.8 hr	X	X	
99	lab sea	30 min	X	X	
100	lab sea	1 hr	X	X	
101	lab sea	40 min	X	X	
102	lab sea	24 hr	X	X	
103	lab sea	65 hr	X	X	
104	lab sea	161 hr	X	X	
105	lab sea	50 min	X	X	X
106	lab sea	50 min	X	X	X
107	lab sea	50 min	X	X	
108	lab sea	30 min	X	X	
109	nat. sea	50 min	X	X	
110	nat. sea	50 min	X	X	
111	nat. sea	50 min	X	X	
112	nat. sea[2]	50 min	X	X	
113	nat. sea[1]	10 min	X	X	
114	nat. sea[1]	15 min	X	X	
115	nat. sea[1]	22 min	X	X	
116	nat. sea[1]	5 min	X	X	
117	nat. sea[1]	3 min	X	X	
118	see note 2			X	X
119	see note 3			X	

SAMPLE NO.	ELECTROLYTE	TIME	STEEL COUPLE	SEM	X-RAY
120	lab sea[3]	30 min	X	X	
121	nat. sea[3]	30 min	X	X	
122	lab sea[3]	10 min	X	X	
123	nat. sea[3]	10 min	X	X	
124	dist. water[3]	3 hr	X	X	

Note 1. - Temperature $= 50^{\circ}C$

Note 2. - MARZ Grade zinc sample (00.999% zinc)

Note 3. - Etched Samples

APPENDIX A

ASTM Standard D1141-52/Standard Specification for Substitute Ocean Water.

1. Scope

1.1 This specification covers the preparation of solutions containing inorganic salts in proportions and concentrations representative of ocean water.

Note 1 - Since the concentration of ocean water varies with sampling location, the gross concentration employed herein is an average of many reliable individual analyses. Trace elements, occurring naturally in concentrations below 0.005 ppm, are not included.

1.2 This specification provides three stock solutions, each relatively concentrated but stable in storage. For preparation of substitute ocean water, aliquots of the first two stock solutions, with added salt, are combined in larger volume. An added refinement in adjustment of heavy-metal concentration is provided by the addition of a small aliquot of the third stock solution to the previous solution.

2. Application

2.1 This substitute ocean water may be used for laboratory testing where a reproducible solution simulating

sea water is required. Examples are for tests on oil contamination, detergency evaluation, and corrosion testing.

Note 2 - The lack of organic matter, suspended matter, and marine life in this solution does not permit unqualified acceptance of test results as representing performance in actual ocean water. Where corrosion is involved, the results obtained from laboratory tests may not approximate those secured under natural testing conditions which differ greatly from those of the laboratory, and especially where effects of velocity, salt atmosphere, or organic constituents are involved. Also the rapid depletion of reacting elements present in low concentrations suggests caution in direct application of results.

3. Reagents

3.1 Purity of Reagents; Reagent grade chemicals shall be used in all tests. Unless otherwise indicated, it is intended that all reagents shall conform to the specifications of the committee on Analytical Reagents of the American Chemical Society, where such specifications are available. Other grades may be used, provided it is first ascertained that the reagent is of sufficiently high purity to permit its use without lessening the accuracy of the determination.

3.2 Purity of Water; Unless otherwise indicated, references to water shall be understood to mean reagent water conforming to ASTM Specification D 1193, for Reagent Water.

3.3 Sodium Hydroxide Standard Solution (1.10N); Prepare and standardize as directed in ASTM Methods E 200, for Preparation, Standardization, and Storage of Standard Solutions for Chemical Analysis.

3.4 Stock Solution No. 1 - Dissolve the indicated amounts of the following salts in water and dilute to a total volume of 7.0 liters. Store in well-stoppered glass containers.

$MgCl_2 \cdot 6 H_2O$	3889.0g
$CaCl_2$ (anhydrous)	405.6g
$SrCl_2 \cdot 6 H_2O$	14.8g

3.5 Stock Solution No. 2 - Dissolve the indicated amounts of the following salts in water and dilute to a total volume of 7.0 liters. Store in well-stoppered glass containers.

KCl	486.2g
$NaHCO_3$	140.7g
KBr	70.4g
H_3BO_3	19.0g
NaF	2.1g

3.6 Stock Solution No. 3 - Dissolve the indicated amounts of the following salts in water and dilute to a total volume of 10.0 liters. Store in well-stoppered amber glass containers.

$Ba(NO_3)_2$	0.994g
$Mn(NO_3)_2 \cdot 6\ H_2O$	0.546g
$Ca(NO_3)_2 \cdot 3\ H_2O$	0.396g
$Zn(NO_3)_2 \cdot 6\ H_2O$	0.151g
$Pb(NO_3)_2$	0.066g
$AgNO_3$	0.0049g

Note 3 - To make the addition of $AgNO_3$ in the above solution, dissolve 0.049g of $AgNO_3$ in water and dilute to 1 liter. Add 100ml. of this solution to stock solution No. 3 before diluting to 10.0 liters.

4. Preparation of Substitute Ocean Water

4.1 Dissolve 245.34g of sodium chloride (NaCl) and 40.94g of anhydrous sodium sulfate (Na_2SO_4) in 8 to 9 liters of water. Add slowly with vigorous stirring 200ml of stock solution No. 1 and then 100ml of stock solution No. 2. Dilute to 10.0 liters. Adjust the pH to 8.2 with 0.1 N sodium hydroxide (NaOH) solution. Only a few milliliters of (Na OH) solution should be required.

Note 4 - The solution should be prepared and the pH adjusted immediately prior to use.

5. Preparation of Substitute Ocean Water with Heavy Metals

5.1 Add 10 ml of stock solution No. 3 slowly, and with vigorous stirring, to 10.0 liters of the substitute ocean water prepared as described in section 4.

APPENDIX B

Scanning Electron Microscope

The introduction of the Scanning Electron Microscope (SEM) in the recent past has enabled the Materials Science field to have available a valuable new technique which overcomes to a great extent many of the limitations of optical and conventional electron microscopes. [16] One great advantage of the SEM besides the availability of much higher magnification (up to 20,000X) is high depth of field. This makes flat specimens unnecessary and makes SEM pictures look "natural." The SEM also gives the scientist an ability to detect regions of different electric charge in a specimen, to examine opaque specimens, and to produce stereoscopic images.

The operating principle of the SEM is closely related to a conventional electron microscope. An electron gun produces a beam of electrons at a diameter of about 50µm. This beam is reduced by two condensing lenses and a final lens which are electrostatic in nature. The final size of the beam is about 100A (or 10µm). An extremely small aperture at about 0.25 degrees imparts a great depth of field which is a major feature of the SEM as described above.

The beam of electrons is caused to scan over the surface of the specimen by two pairs of deflection plates which move the beam in a raster pattern similar in many respects to the raster pattern principle used in television. As the electron beam strikes the specimen, secondary electrons are emitted as are back scattered electrons, X-rays, light, and Auger electrons. The actual magnitude of secondary electron emission depends upon the angle between the beam and local surface as well as the chemical content of the surface. The secondary electrons are utilized to form the image.

The secondary electrons emitted are detected in an electron collection system which contains a scintillator and photo-multiplier and are amplified and displayed on a cathode ray tube. The beams of the cathode ray tube and the SEM electron gun are synchronized for the scanning process. The ratio of the length of the scan line on the cathode ray tube on the length of a scan line on the specimen is the magnification of the image.

One of the most important features of the SEM image with respect to this study is the electrical distinction between light and dark areas on the image. Light areas indicate less conductive areas and vice versa for dark areas.

An attachment to the SEM utilized in these studies is
a Princeton Gamma-Tech PGT 1000 X-ray Analyzer. The micro-
scope and analyzer perform as an integral unit. Character-
istic X-rays are emitted by elements in a sample when that
sample is "fluoresced" by higher energy radiation (gamma
rays, X-rays or charged nuclear particles). These X-rays
are detected by a solid state Si(Li) semiconductor detector.
The detector converts each X-ray photon into electron-hole
pairs. The number is proportional to the energy of the
X-ray photon. Electronic circuits convert these electron-
hole pairs into voltage pulses that are sorted according
to energy by means of a pulse height multichannel analyzer.
Clusters of the voltage pulses form gaussian-shaped peaks
and these peaks are displayed by the multichannel analyzer.
The position of the peaks on the horizontal scale corresponds
to X-ray energy and consequently affords a direct means of
identification of the element represented by the peak. The
ar'a under the peak (number of X-ray events of a particular
energy) is a function of the concentration of that element.

APPENDIX C

Chemical Polishing of Zinc for Etching Purposes [16]

An easy alternative to mechanical polishing and electro-polishing of zinc and its alloys is the chemical polishing process. Chemical polishing is distinct from "electrolytic" polishing (electropolishing) since some metal surfaces can be polished by immersion in a suitable solution without the application of an external potential. The function of an ideal chemical polishing process is:

(a) smoothing of the surface irregularities;

(b) brightening without the appearance of etch pits. In general, the rates of dissolution are much higher in chemical polishing than for electropolishing, and rough surfaces can be smoothed rapidly.

The following solution was used for chemical polishing the zinc samples in this study:

> 200g chromic acid
>
> 15g sodium sulfate
>
> 50ml nitric acid
>
> 950ml water

The samples were immersed in the above solution for times varying from several minutes to thirty minutes. The longer the sample was immersed, the heavier the etch. An immersion

of five minutes was found to be an optimum time for the particular zinc alloy used. Following immersion in the above solution, the samples were rinsed in a dilute chromic acid solution (half chromic acid, half distilled water) and then rinsed in distilled water. The samples subsequently were rinsed in alcohol in order to negate the chromic acid film remaining from the etching process above. All the rinsing described above is necessary because a dense layer is formed during the initial immersion which is soluble in water. The rate of dissolution during the chemical process is reported to be approximately 7 microns/minute.

LIST OF REFERENCES

1. G. Butler, H. Ison, Corrosion and its' Prevention in Waters, 1966, Reinhold Publishing Corporation.

2. R. C. Weast, "Surface Characteristics of Zinc in Aqueous Media," Final Report ILZRO Project ZE-20, International Lead Zinc Research Organization Inc., May 1967.

3. B. H. Tytell, H. S. Preiser, "Cathodic Protection of an Active Ship Using Zinc Anodes," ASNE Journal, Nov. 1956, pp. 701-704.

4. Humphrey Davy, "On the Corrosion of Copper Sheathing on Ships by Sea Water, and a Method of Preventing This Effect; and in Their Application to Ships of War and Other Ships," Phil. Trans. Ray. Soc. (London), 1824; Corrosion, 3, 295 (1947).

5. Sigmund Schuldines, The Cathodic Protection of Ships Hulls in Sea Water - A Critical Review of the Problem. Naval Research Laboratory Report #3616, pages 25-32, (1950) January.

6. D. B. Anderson and R. B. Teel, "The Effect of Iron in Galvanic Zinc Anodes in Sea Water, " Corrosion, 12 (1956), 53-59.

7. R. T. Southin, "Some Observations on the Microstructure of Zinc Alloy Anodes," J. Inst. Metals 93 (1964-65) 428.

8. L. J. Waldron, M. H. Peterson, "Effect of Iron, Aluminum and Cadmium Additions On the Performance of Zinc Anodes in Sea Water," Corrosion, 16 (1960), 375-379.

9. J. A. H. Carson, W. L. M. Phillips, J. R. Wellington, "A Laboratory Evaluation of Zinc Anodes in Sea Water," Corrosion, 16 (1960), 171-177.

10. R. A. Bornholdt, J. Perkins, "SEM Examination of Corrosion Product Morphology for Anodically Polarized Zinc," _Metallography_ 8, 39-47, (1975)

11. R. A. Bornholdt, J. Perkins, "Corrosion Product Morphology in Anodic Electrocrystallization of Zinc Oxide on Zinc," _Corrosion Science_ (in press, 1975).

12. N. T. Monney, "Deep Ocean Corrosion - Simulation Facilities vs. In-Situ Research," _Materials Protection and Performance_, Vol. 12, No. 1, Jan. 1973.

13. A. Brasunas, "A Critical Review of the Reproducibility and Interpretation of Corrosion Test Procedures," _Materials Protection_, December, 1967, 20-24.

14. Military Specification MIL-A-18001H, _Anodes, Corrosion Prevention, Zinc; Slab, Disc, and Rod Shaped_, 28 June 1968.

15. R. A. Bornholdt, _Corrosion Product Morphology on Zinc Anodes in Sea Water_, MSME Thesis, Naval Post-graduate School, June 1974.

16. W. J. McG. Tegart, _The Electrolytic and Chemical Polishing of Metals in Research and Industry_, 2nd ition, p. 96-102, Pergaman Press, 1959.

17. J. V. Petrocelli, _Electrochemistry of Dissolution Processes_, The Surface Chemistry of Metals and Semiconductors, John Wiley & Sons, Inc., 1960, pp. 326-356.

18. B. E. Conway, _Theory and Principles of Electrode Processes_, 1965, The Ronald Press Co., pp. 187-200.

INITIAL DISTRIBUTION LIST

No. Copies

1. Defense Documentation Center   2
   Cameron Station
   Alexandria Virginia   22314

2. Library, Code 0212   2
   Naval Postgraduate School
   Monterey, California   93940

3. Department Chairman, Code 59   1
   Department of Mechanical Engineering
   Naval Postgraduate School
   Monterey, California   93940

4. Professor A. J. Perkins, Code 59Ps   4
   Department of Mechanical Engineering
   Naval Postgraduate School
   Monterey, California   93940

5. LT James M. Toda, USN   1
   5257 North Lake Road
   Virginia Beach, Virginia   23454